Design, Characterization, and In Vivo Applications of a Novel, Concentric, Hybrid micro-ECoG Array

by

Ian Akamine

A Dissertation Presented in Partial Fulfillment
of the Requirements for the Degree
Doctor of Philosophy

Approved January 2024 by the
Graduate Supervisory Committee:

Jennifer Blain Christen, Chair
Michael Goryll
James Abbas
Stephen Helms Tillery
Jit Muthuswamy

ARIZONA STATE UNIVERSITY

May 2024

ABSTRACT

Neurological disorders are the leading cause of physical and cognitive decline globally and affect nearly 15% of the current worldwide population. These disorders include, but are not limited to, epilepsy, Alzheimer's disease, Parkinson's disease, and multiple sclerosis. With the aging population, an increase in the prevalence of neurodegenerative disorders is expected. Electrophysiological monitoring of neural signals has been the gold standard for clinicians in diagnosing and treating neurological disorders. However, advances in detection and stimulation techniques have paved the way for relevant information not seen by standard procedures to be captured and used in patient treatment. Amongst these advances have been improved analysis of higher frequency activity and the increased concentration of alternative biomarkers, specifically pH change, during states of increased neural activity. The design and fabrication of devices with the ability to reliably interface with the brain on multiple scales and modalities has been a significant challenge.

This dissertation introduces a novel, concentric, multi-scale micro-ECoG array for neural applications specifically designed for seizure detection in epileptic patients. This work investigates simultaneous detection and recording of adjacent neural tissue using electrodes of different sizes during neural events. Signal fidelity from electrodes of different sizes during in vivo experimentation are explored and analyzed to highlight the advantages and disadvantages of using varying electrode sizes. Furthermore, the novel multi-scale array was modified to perform multi-analyte detection experiments of pH change and electrophysiological activity on the cortical surface during epileptic events. This device highlights the ability to accurately monitor relevant information from multiple electrode sizes and concurrently monitor multiple biomarkers during clinical periods in one procedure that typically requires multiple surgeries.

DEDICATION

This dissertation is dedicated to my family, who has been there and supported me throughout my journey, and especially my girlfriend, Kaylee, whose patience, enouragement, love, and support i could not do without.

ACKNOWLEDGMENTS

Thank you so much to Dr. Jennifer Blain Christen for the opportunity and resources to pursue the research outlined in this dissertation and the support along the way.

Thank you also to my committee members: Dr. Micheal Goryll, Dr. Jit Muthuswamy, Dr. Stephen Helms Tillery, and Dr. James Abbas for all the advice, guidance, and feedback during my time here.

Thank you to all the members, past and present, of the BEST lab group who have made this journey special through their assistance inside and outside of the lab and most importantly their friendship.

Last but certainly not least, thank you to my family: my parents for all you have done in your support of me throughout my academic and personal life. My brother Joshua, for all the memories we have made during my time not thinking about school. And most importantly my amazing partner Kaylee, the love and support you have shown me has been undeniable and no words can express how thankful i am to have you by my side.

TABLE OF CONTENTS

Page

LIST OF TABLES

LIST OF FIGURES

Figure Page

Chapter 1

INTRODUCTION

The human nervous system, consisting of the central and peripheral nervous systems, is essential for regulating and coordinating bodily functions, maintaining homeostasis, and adapting to different environments. Its ability to sense, process, and respond to stimuli has made it a crucial area of research in neuroscience and medicine (Tortora and Derrickson 2020). Disorders in the nervous system from birth or by injury and disease continue to be one of the most researched yet unsolved mysteries in medicine. Nervous system disorders often lead to the loss of bodily function and impact lives in areas that most take for granted. A few examples of common neurological disorders, their prevalence, causes, and symptoms are shown in Table 1. Many of the most common disorders have cost the United States almost 800 billions of dollars a year and have severely impacted the lives of those diagnosed and their families (Feigin et al. 2021). Employing medical devices, and specifically brain computer interfaces (BCI's), with the ability to interact and decode information from the brain has become paramount in determining therapies and hopefully one day, cures to these debilitating conditions.

One of the most commonly researched BCI has been the neural electrode. Many types of neural interfacing technologies (Fig.1) have shown success in diagnosing the aforementioned neurological disorders. A few of these technologies include electroencephalography (EEG), electrocortiography (ECoG), magnetocephalography (MEG), functional magnetic resonance imaging (f-MRI), and deep brain stimulation (DBS) (Shih, Krusienski, and Wolpaw 2012). Although most non-invasive technologies are

Table 1. Common Neurological Disorders and Their Prevalence, Causes, and Symptoms

Neurological Disorder	**Prevalence**	**Cause**	**Symptoms**
Autism	1 in 36 children in the U.S/ 1 in 100 worldwide	Genetic and environmental	Problems with social communication and interaction, restricted and repetitive behaviors
Multiple Sclerosis (MS)	380,000	Degeneration	Muscle weakness, visual and sensation problems
Traumatic Brain Injuries (TBI's)	Over 75,000 TBI deaths/year	Trauma	Loss of consciousness, headache, confusion
Epilepsy	3 million	Genetic factors, trauma	Jerking movements in arms and legs, loss of consciousness
Parkinsons	1 million	Degeneration	Tremors, impaired posture, balance problems
Alzheimers	6.5 million (aged 65 and older)	Degeneration	Memory loss
Stroke	795,000 people diagnosed with a stroke/year	Vascular disease	Sudden numbness or weakness, trouble speaking and moving

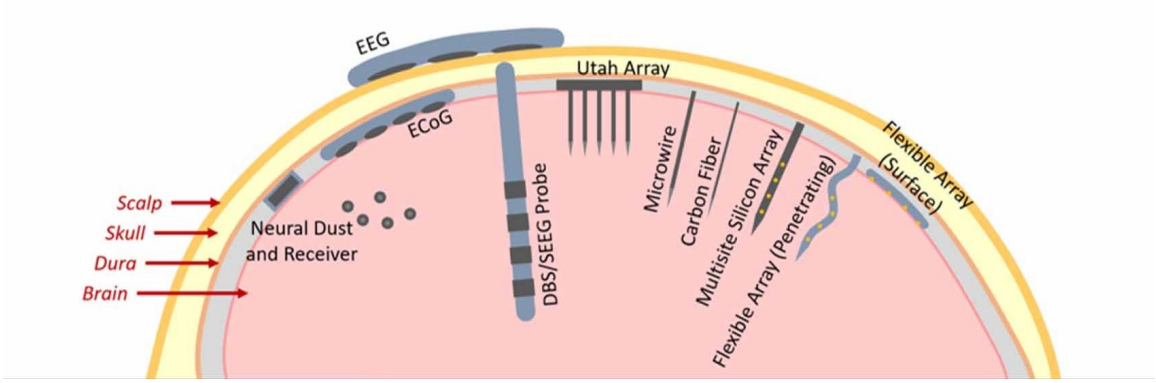

Figure 1. The major types of implantable neural interfaces in the brain. Taken from (Thielen and Meng 2021)

harmless, as we approach 100 years since the first EEG was ever recorded (Haas 2003), we have learned that these non-invasive technologies provide limited signal quality. Improving the level of care requires an increase in the quality of recorded signal that can only be acquired through an implantable neural device (Clark et al. 2010). Due to the scale required of an implantable device, improving the electrode design and electrode properties is crucial to improving the quality of the acquired signal. Characteristics such as low signal-to-noise ratio (SNR), biocompatibility, and ultra-flexibility in order to conform to the curvature of the brain are all highly desirable qualities of implantable electrode arrays (Ortiz-Catalan et al. 2012; Geddes and Roeder 2003; Takashi D Yoshida Kozai et al. 2012). These factors have a significant impact on the diagnosis and treatment of neurological disorders. Optimizing the functionality of implantable neural electrodes relies heavily upon the materials from which they are designed and fabricated. Technological breakthroughs in micro-and nanofabrication techniques have revolutionized the way current microeletrode arrays (MEAs) are designed, enabling the creation of high-density arrays with miniaturized electrodes, reduced electrode spacing, and increased spatial resolution (Obien et al. 2015).

In an effort to improve the diagnosis and treatment of those with neurological

disorders, electrode arrays have become increasingly smaller to increase the electrode density for an enhanced spatial mapping of the regions of interest. Pioneering work in neural recording and stimulation began with the advent of microwire arrays. Microwire arrays are bundles of microwires traditionally made of insulated metal, typically Pt, stainless steel (SS), and/or tungsten (W), with an exposed tip for recording or stimulation. Microwires are designed and employed to record from individual neurons and estimate the position of these neurons by triangulation (Prasad and Sanchez 2012). Although microwires were and remain invaluable tools in neuroscience research, limitations on scalability and integration density persist(Wise et al. 2008). Breakthroughs in microfabrication techniques such as photolithography and thin-film deposition paved the way for thin-film arrays such as silicon-based arrays and flexible MEAs (Fig. 1). These advances in microfabrication enabled higher density electrode arrays, more precise neural probe designs, improvements in biocompatibilty, and the integration of microelectronics into implantable devices, enhancing recording capabilities. The Utah and Michigan arrays are two seminal designs of silicon-based arrays still in use today (Campbell et al. 1991; Kipke et al. 2003). The Michigan array's design allows for multiple-site neural recordings, enabling simultaneous monitoring of neural activity across the length of the array shaft achieving enhanced spatial resolution and signal fidelity (Wise et al. 2008). On the other hand, the Utah array was designed as a rigid array consisting of up to 256 conductive silicon needle-like electrodes. Characterized by its higher electrode count and organized assembly, the Utah array offered dense multi-site recordings enabling precise neural interfacing, opening the possibility of detailed investigations of neuronal assemblies and advanced BCIs. However, the recording sites of the Utah array are limited to the tips of the conductive needles due to the restrictive design of the array.

Building upon the designs of the Michigan and Utah arrays, a paradigm shift in neural electrode design took place when advances in microfabrication introduced flexible MEA's as an upgraded alternative from the silicone-based arrays. The rigid architecture of the Michian and Utah arrays elicited high tissue damage and chronic inflammation because of their material mismatch, more specifically the difference in mechanical stiffness of the implantable devices and the neural tissue (Takashi D. Y. Kozai et al. 2015). Young's modulus is the measure of the stiffness of a material and one of the most prominent parameters during material selection. For reference, silicon has a Young's modulus of $\sim$ 170 GPa while neural tissue has a Young's modulus of $\sim$ 3 kPa (Cheung 2007). This massive mismatch contributes to inflammation at the implantable site and induces the foreign body response. Glial scar formation around the implantable device is often a result of this foreign body response and reduces the conductive performance of the electrode. The introduction of flexible MEAs revolutionized neural electrode designs by incorporating flexible substrates such as polyimide (PI), parylene-C, polyurethane (PU), and polydimethylsiloxane (PDMS) and all have Young's modulus values that are two orders of magnitude lower than metals and silicon (He, Dong, and Qi 2020). The flexibility of these MEAs allows them to conform to the irregular topography of the neural tissues, reducing tissue damage and improving long-term stability. By minimizing the foreign body response, and encouraging more favorable tissue-electrode interactions, flexible MEAs also exhibit improved biocompatiblity and enhanced signal fidelity (Luan et al. 2017; Khodagholy et al. 2013). The extremely modifiable properties of the substrate materials used in fabricating flexible MEA's has greatly progressed increasing the electrode density while reducing the overall size and thickness of MEAs (Viventi et al. 2011; Khodagholy et al. 2015; Tybrandt et al. 2018). Flexible MEAs have been able to employ traditional

electrode materials as substrate materials while also incorporating specialized coatings to promote better biointegration, reduced impedance, and minimiznig tissue reactions (Polikov, Tresco, and Reichert 2005).

Historically, traditional noble metals such as platinum (Pt), gold (Au), and iridium (Ir) have dominated the landscape owing to their exceptional electrical conductivity, biocompatibility, and stability (Wang et al. 2023). However, just like the rigid structure of the aforementioned silicone-based arrays, their rigidity has faced challenges with tissue damage, chronic inflammation, and signal degradation over time. Achieving quality signal detection and signal delivery while minimizing tissue response has been a large hurdle for implantable neural interfaces. In response to this, researchers aimed to mitigate the effects of tissue damage and improve biocompatibility through insulating materials to coat said metal electrodes. However, problems with mechanical stability remained (G. Kim et al. 2018). With the advent of flexible MEAs and polymer-based materials like PI and parylene-C, these materials also gained prominence for their roles as electrode coatings (D.-H. Kim et al. 2010). As microfabrication techniques permitted the design smaller electrodes, this inherently increased their impedance. Organic and inorganic coatings were introduced to address this impedance increase while also limiting the tissue response (Green and Abidian 2015). Conductive polymers (CP's) such as poly(3,4-ethylenedioxythiophene) (PEDOT), carbon-based materials like glassy carbon and carbon nanotubes (CNTs), and conducting hydrogels (CH's) are a few examples of organic materials that have enhanced the performance and biocompatibility of microelectrodes. Inorganic materials like Pt-Black, iridium oxide (IrOx), and titanium nitride (TiN) have provided robustness, stability and exceptional electrical properties vital for precise neural recordings (Aregueta-Robles et al. 2014).

Just as the electrode material itself is important in signal transduction, so are the electrode coatings.

With the ever increasing channel count of microelectrode arrays and the broadening of possible neural electrode designs, BCIs have taken on a heavier responsibility when it comes to detecting neural activity. One of the significant disorders that relies heavily upon the accurate and precise detection of abnormal neural activity is epilepsy. Epilepsy is one of the most common prevalent neurological disorders and is defined by a state of recurrent and spontaneous seizures (Scharfman 2007). Seizures are characterized as the disruption of the mechanisms that create balance between inhibition and excitation in the brain. This disruption is seen as a clinical manifestation of an abnormal and excessive discharge of a population of cortical neurons (Bromfield, Cavazos, and Sirven 2006). Although a cure for epilepsy remains to be found, BCI's such as EEG, ECoG, and µ-ECoG have enabled clinicians to successfully diagnose and develop treatments. Sadly, one-third of all epilepsy patients are unable to resolve their complications through medication and fall under the category of "drug-resistant epilepsy", leading to surgical intervention. Due to the potential complications associated with such a procedure, accurately defining the seizure onset zone (SOZ) and the breadth of the epileptogenic tissue is paramount (Kalilani et al. 2018).

Traditionally, seizure monitoring had relied upon scalp EEG as the fundamental technique to detecting abnormal patterns indicative of seizures. Neuroimaging techniques like magnetic resonance imaging (MRI) and computer tomography (CT) were employed as complimentary diagnostic tools to identify structural abnormalities linked to seizures (Roy and Pandit 2011; Ho et al. 2013; Ramgopal et al. 2014; Beniczky et al. 2018; Ein Shoka et al. 2023). Intracortical monitoring using clinical macro

electrodes like subdural grids and strips or clinical ECoG arrays represented a seismic shift in understanding the dynamics of seizure activity by providing broader coverage of brain areas and more precise and continuous monitoring of neural activity (Behrens et al. 1994; Adelson et al. 1995; Voorhies and Cohen-Gadol 2013; Sweet et al. 2013). Although intracortical macro electrodes have improved the spatial resolution of seizure activity recorded across neural networks when compared to scalp EEG, the neural activity captured from these clinical electrodes typically consists of activity < 70 Hz. Utilizing microelectrode arrays has contributed significantly to furthering our understanding of epileptic mechanisms. The smaller size of micro electrodes has exponentially enhanced the spatial resolution compared to its macro counterpart by enabling recordings at the level of individual neurons or small neuronal populations (Park et al. 2020; Gupta, Grover, and Abel 2020; Dai et al. 2021). Micro electrodes have also been instrumental in detecting and analyzing high frequency oscillations in the brain (Zijlmans et al. 2012; Jacobs et al. 2012; Jiruska et al. 2017). HFOs specifically in the range of 80-500 Hz have been considered biomarkers for the epileptogenic area and a significant aid in precisely localizing the SOZ (Jiruska and Bragin 2011; Jacobs et al. 2012; G. Worrell et al. 2012). Successful detection of neural activity using both clinical macro electrodes and micro electrodes has paved the way for the use of hybrid electrodes . Integrating both micro and macro features, hybrid electrodes aim to combine the advantages of high-resolution micro electrodes with broader coverage similar to macro electrodes. Simultaneous monitoring using hybrid electrodes has provided clinicians with a unique opportunity to collect information on broad, network level dynamics from clinically-sized macro electrodes with the localized, cellular dynamics only found on micro electrodes (Stead et al. 2010). HFOs and micro seizure information obtained on micro electrodes could potentially provide the

interictal biomarker of epileptogenesis that localizes the SOZ in ways macro electrodes simply could not (Van Gompel et al. 2008; Chari et al. 2020; Sun et al. 2022).

The success of hybrid electrode arrays and other BCIs in neural monitoring, along with major advances in technology, has propelled researchers to explore integrating multiple modalities in efforts to provide a more holisitic understanding of epilepsy. Typical efforts of multi-modal monitoring have centered around simultaneous electrophysiological recording and neural imaging enabled by conductive, transparent microelectrode arrays (Mulcahey et al. 2022; Tian et al. 2022). Yet, as we learn more about the biological phenomena that occur during seizures, detecting the change in concentration of certain chemicals has correlated well with the electrical discharges of seizure activity (Raimondo et al. 2015; González et al. 2019). One of the most prominent biomarkers of homeostasis and proper neural functioning is pH. Neural excitability is greatly influenced by the acid-base equilibrium and significant disturbances to equilibrium could lead to epileptic activity (Rho 2009; Pavlov et al. 2013)). Studies over the years have highlighted that induction of seizures have elicited pH changes of at least 0.41 units (Siesjö et al. 1985; Rho 2009; Raimondo et al. 2015; Lu et al. 2021). Although most seizures stop spontaneously, the molecular mechanisms for this remain cloudy. Typical anti-epileptic drugs (AEDs) work by inhibiting voltage-gated sodium or potassium channels in an effort to prevent overexcitation (Macdonald 1995, Czapinski 2005, Gsills 2020). However, Ziemann et al. (2008) discovered that acid-sensing channel-1a (ASIC1a), a small ion channel with exquisite pH sensitivity and neuron excitability regulator, could be disrupted to shorten seizure duration and prevent progression. These findings showed that there are alternative strategies and suggest the potential for new therapeutic strategies to combat epilepsy.

In this dissertation, the detailed fabrication process and benchtop characterization

of a novel, concentric, multi-scale micro-ECoG array is outlined in Chapter 2. Chapter 3 examines the *in vivo* capabilities of the multi-scale array in monitoring somatosensory evoked potentials (SSEP's) and pilocarpine-induced seizures. Chapter 4 describes the ability of the multi-scale array to perform multi-modal monitoring of pH and electrical activity in a live animal model. Conclusions of this work and future recommendations are highlighted in chapter 5.

Chapter 2

DESIGN AND FABRICATION OF THE CONCENTRIC MULTI-SCALE ARRAY

2.1 Design Process

Clinicians inspired the design of the hybrid, multi-scale array to keep clinical translation simple by maintaining the size and overall area of standard clinical electrodes while adding high-resolution sensing of the same cortical regions. The definable electrode geometries and patterns were designed using L-Edit and SOLIDWORKS, and once created, the pattern was printed onto a chrome mask for patterning with UV light exposure onto the wafer. The novelty of our hybrid design stems from the three electrode geometries embedded in this concentric "telescopic" design, which we have called the macro, mesos, and micros. The macro electrode was designed to directly compare to clinical subdural ECoG grid electrodes, with a 4 mm diameter. Micros were designed to span a single cortical column and mimic recordings from typical neural microelectrodes. These micros have a diameter of 40 µm and a center-to-center pitch of 350 µm, as G. Worrell et al. (2012) suggested. Mesos were designed as an intermediary electrode to bridge the size gap between the macro and micros with a 1 mm diameter and 1.5 mm center-to-center spacing.

The macro and meso sized electrodes were included in the array design for a dual-purpose of recording and stimulation. Electrical stimulation of the cortex for mapping purposes has been used for many years (Lüders et al. 1988). Cortical stimulation induced seizures has been a polarizing methodology in the localization of the epileptogenic region (Kovac, Kahane, and Diehl 2016). Research has shown that

cortical stimuli may provoke epileptiform afterdischarges, which can then progress to clinical seizures (Ellrich 2020). These afterdischarges are defined as preliminary stages of epilepsy and used as models of epileptic activity. When stimulation produces afterdischarges, additional bursts of stimuli were applied to prove the effectiveness in aborting afterdischarges. Results indicated that the stimulation of epileptogenic regions significantly shortened or terminated future epileptiform discharges (Kinoshita et al. 2005; Enatsu et al. 2012). In addition to proving the recording capabilities of our multi-scale concentric design, we aim to provide proof that the multi-scale array is capable of evoking motor responses through cortical stimulation.

The array comprises 32 electrodes: 1 macro, four mesos, and 27 micros, covering an area of 12 mm^2. The recording system interfaced with the multi-scale array through a connection made with a 39-pin zero insertion force (ZIF) connector (Molex Connector Company, Lisle, IL, USA) soldered to a custom-designed flexible printed circuit board (FPCB). 127-µm thick polyether ether ketone (PEEK) strips were adhered to the back of the multi-scale array to maintain consistent contact with the ZIF connector on the FPCB.

2.2 Nanofabrication Process

Fabrication of the multi-scale hybrid electrode array was conducted at Arizona State University in two cleanroom facilities: a Class 100 cleanroom and a Class 1000 cleanroom for separate portions of the fabrication process. The process commenced with cleaning a sacrificial silicon wafer by placing it in an acetone-filled beaker and manually agitating for 30 seconds, removing it and placing it in an isopropyl alcohol (IPA)-filled beaker and agitating for another 30 seconds, removing it and placing it

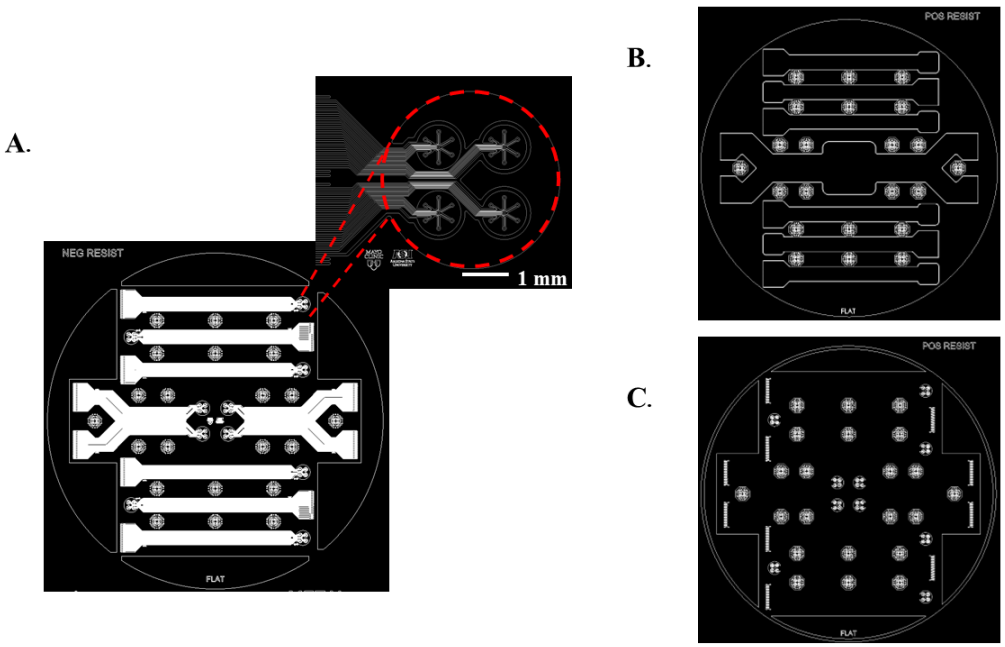

Figure 2. Mask design: A. Metallization mask defining the metal patterns of the multi-scale array. Inset: showing zoomed in image of the electrode area. B. The cutout mask defines the area around the array the femtosecond laser will cut on for array removal. C. The opening mask defines the exposed regions of metal- the electrodes and the connector pads.

in a deionized (DI) water filled beaker, and lastly drying with a nitrogen gun. An anti-adhesion layer of VM-651 diluted with DI water was spin-coated at 3000 rpm onto the wafer and dried. Then, PI-2611 polyimide was spin-coated for 30 seconds at 2500 rpm and soft-baked on a hot plate at 90 °C to create a 10-micron substrate layer. Next, photolithography was conducted by spinning AZ nLOF 2020 photoresist at 3000 rpm for 30 seconds, then soft baked on a hot plate at 110 °C for 60 seconds, followed by UV exposure using an OAI 808 aligner beneath a chrome mask shown in Fig. 2, developed in AZ 300 MIF solution with slight agitation, and rinsed with DI water. Following a two-minute oxygen descum to roughen the surface using a PlasmaTherm PT-790 Reactive Ion Etching (RIE), a Lesker PVD75 e-beam evaporator was used to deposit a 5 nm layer of titanium (Ti) and a 100 nm layer of platinum (Pt) by electron

beam evaporation. Electron beam evaporation is a process by which a beam of emitted electrons from a heated tip is aimed at a metal-filled crucible within a vacuum chamber that heats the metal until it evaporates and diffuses, creating a uniform layer of the target metal atop the wafer. After removing the wafer from the e-beam evaporator, metal lift-off is performed using AZ 400T photoresist stripper, rinsed with DI water, and dried in an oven for 30 minutes. Before insulation deposition, conductive metal testing is performed using a four-point probe measuring the resistance of the metal. After ensuring the metal layer is conductive, an additional two-minute oxygen descum using the PlasmaTherm PT-790 RIE is completed to roughen the polyimide surface and improve the adhesion of the subsequent 10 µm polyimide insulation layer. The next layer deposited was another AZ nLOF 2020 photoresist similar to the layer deposited previously and exposed using the same OAI 808 aligner and AZ 300 MIF developer. This process utilized a new chrome mask to pattern the active sites, such as the connector pads and electrode contacts. The PlasmaTherm PT790 RIE tool was used to dry etch through the polyimide insulation, insulating the exposed metal leads. The remaining photoresist was removed through manual agitation in AZ 400T photoresist stripper and IPA and rinsed with DI water. Following photoresist removal and electrode cleaning, the device was cut from the wafer using a UV (342 nm) femtosecond laser (Photomachining, Inc., Pelham, NH) and separated from the wafer. The fabrication steps are summarized in Fig. 4.

The wafers were inspected at various stages throughout the fabrication process, validating the device's integrity before proceeding to the next step. Mechanical tools such as an optical microscope, reflectometer, profilometer, and probe station ensured the fabrication proceeded as planned.

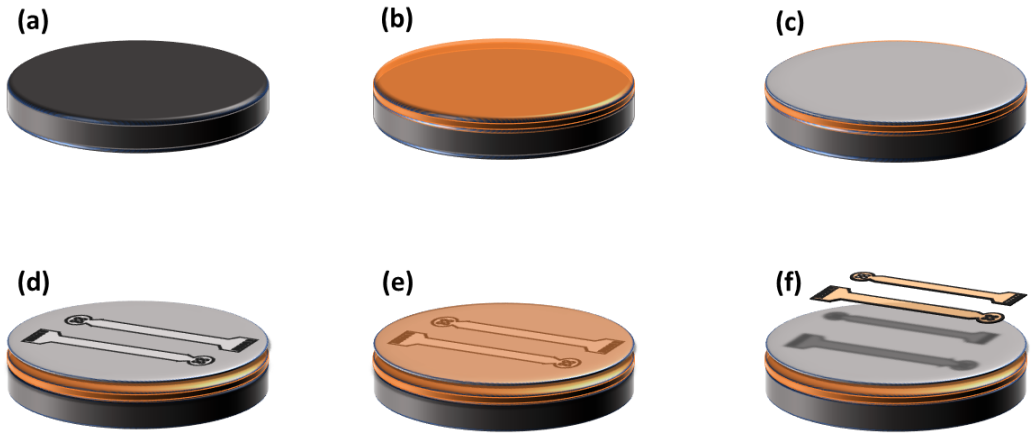

Figure 3. Protocol used to fabricate multi-scale array: (a) silicon wafer; (b) spin polyimide; (c) metal layer deposition; (d) patterning; (e) insulation layer deposition and spin photoresist; (f) pattern, etch and removal of photoresist and release from silicon wafer.

2.3 Electrochemical Characterization

We employed electrochemical impedance spectroscopy (EIS) and cyclic voltammetry (CV) to characterize the electrophysiological properties of the electrodes on the multi-scale array. EIS involves sending an AC signal between an electrochemical cell consisting of a working electrode and counter electrode while measuring the potential drop with respect to a reference electrode and measuring the ratio of voltage to current and the phase difference between the two. We conducted our benchtop characterization using an Admiral SquidStat Plus potentiostat (Admiral Instruments, Tempe, AZ, USA) with a three-electrode chemical cell consisting of the multi-scale electrodes (macro, mesos, and micros) as the working electrode, a 23-cm platinum

coil as the counter electrode (BASi Research Products, West Lafayette, IN, USA), and a 3M NaCl Ag/AgCl electrode as our reference (BASi Research Products) all in a 1x phosphate-buffered saline (PBS) solution. The frequency was swept from 1 MHz to 1 Hz with a 10 mV RMS AC source and a 0.5 V DC offset. The frequency of interest for neural arrays is examined at 1 kHz and showed an impedance of 3.2 $\pm$ 0.2 kΩ for the macro, 4.4 $\pm$ 0.4 kΩ for the mesos, and 212.2 $\pm$ 20.4 kΩ for the micros. Fig. 4 shows an example of the EIS spectra for the multi-scale electrodes and follows what we expected, where the impedance is dominated by capacitive coupling at lower frequencies while being more affected by the series resistance at higher frequencies where the phase approaches zero.

CV was also performed to define the water windows of the electrodes, which assisted in determining the parameters used during the EIS measurements. CV was completed using the SquidStat Plus potentiostat inside a 1x PBS solution with the same three-electrode chemical cell used for the EIS measurements. The working electrodes were the electrodes on the multi-scale array; the 3M NaCl Ag/AgCl electrode was used as a reference, and the platinum coil was used as the counter electrode. The potential was swept across the working electrode from +1 and -1 V at 50 mV/s and repeated three times to achieve sufficient averaging. Figure 5 shows the voltammograms for the macro, meso, and micro electrodes. The curves for all three electrodes follow typical water windows for Pt electrodes, with -0.6 to 0.8 V being standard for Pt electrodes with respect to a Ag/AgCl reference electrode.

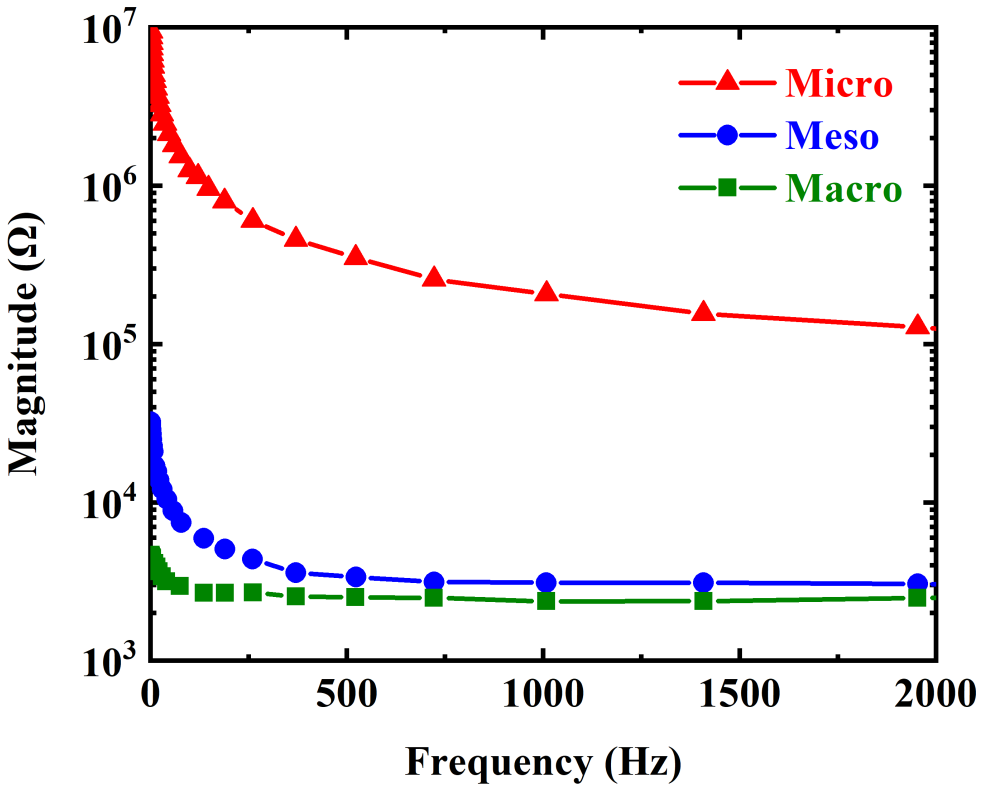

Figure 4. Electrochemical impedance spectroscopy of the three electrode sizes on the 32-channel multi-scale array

2.4 Cross-talk

A common concern regarding thin-film multi-channel microelectrode arrays has been the potential of cross-talk and concern of channel dependence between neighboring channels (Matteucci et al. 2016; Rubehn et al. 2009; Lopez et al. 2014). Cross-talk is undesirable coupling that can originate from resistive, capacitive, and inductive sources, although inductive sources were not considered in this work. Resistive coupling stems from the physical interaction between the electrodes and their traces, while the capacitive coupling arises from the displacement currents induced by the electric field

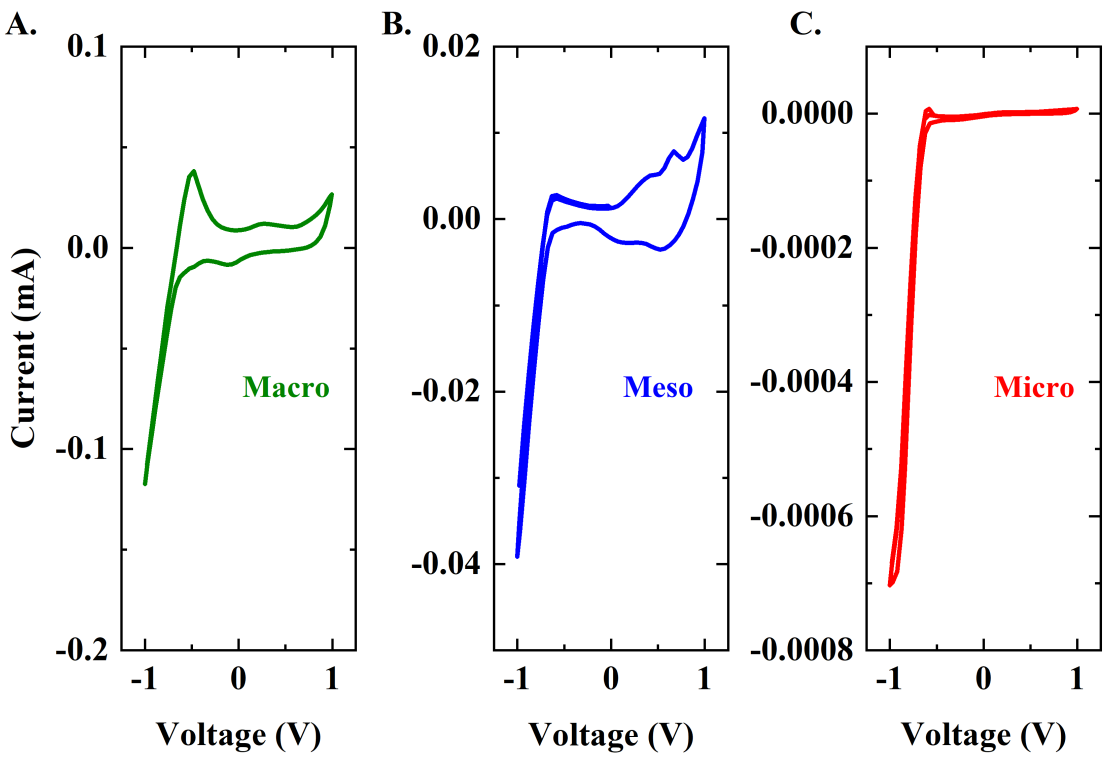

Figure 5. Cyclic voltammograms. A Macro electrode. B. Meso electrode. C. Micro electrode.

across those electrodes and their traces, and increases with frequency (Porto Cruz et al. 2019). Both the resistive and capacitive coupling is influenced by the surrounding medium and the absorption of water from the polymer insulator. Parasitic capacitance between neighboring traces is the primary reason for this potential cross-talk, and scales directly with trace length and inversely with trace separation (Tchoe et al. 2022). This is why we chose to design the array with shorter traces. In essence, cross-talk is influenced by four factors: effects occurring between channels through substrate encapsulation, effects occurring between traces and the surrounding medium, electrode site impedance, and grounding conditions (Cornuéjols et al. 2023).

There remains to be a standardized method for quantifying the cross-talk that

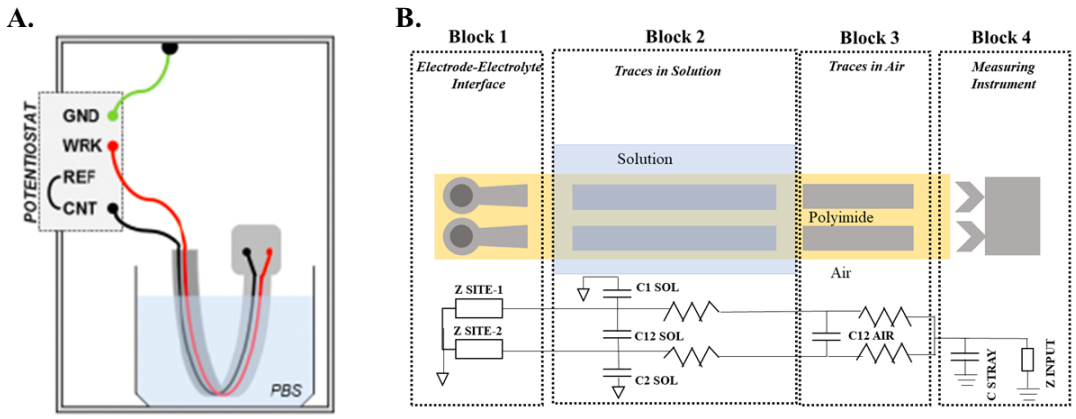

Figure 6. A. Experimental setup used in the impedance sweep. B. Lumped model of a multi-scale array with four blocks: 1) the electrode-electrolyte interface, 2) traces in the solution, 3) traces exposed to air, and 4) the input impedance of the measuring instrument. Parameters: Z SITE-1 and Z SITE-2 represent the impedance of the electrode sites on the array. C1 SOL and C2 SOL represent the leakage capacitance from traces 1 and 2 through the polyimide immersed in solution. C12 SOL and C12 AIR represent the leakage capacitance between traces 1 and 2 through the immersed and non-immersed portions of the array. C STRAY and Z INPUT represent the stray capacitance and input impedance from the measuring instrument. Adapted from (Porto Cruz et al. 2019)

occurs in MEAs. Because of the desire for thinner MEAs with increased channel counts, unconventional electrode designs, and most importantly the pursuit of quantifying higher frequency data, the concern of potential cross-talk and channel interference, as noticed by highly similar electrocortigrams from electrodes with neighboring traces, has steadily increased.

2.4.1 Cross-talk Methods

In order to understand the potential effects of parasitic capacitance within the multi-scale array, we performed impedance sweeps on the multi-scale array using the Squidstat Plus potentiostat. Impedance sweeps were carried out in a 2-electrode cell with the counter and reference electrode shorted with one another and connected to the macro electrode (trace located furthest left on the array if the array is oriented vertically with the electrodes facing forward) and all other 31 electrode traces set as the working electrode, one electrode at a time. Investigating the potential coupling of the electrode traces required bending the electrode concavely and immersing the traces portion of the array in PBS (pH 7.4) as depicted in Fig. 6. This setup enabled us to exclude the electrode-electrolyte interface by removing the electrodes from the PBS solution. Electrode traces were left immersed for an hour prior to taking EIS measurements to allow for drift stabilization from the water absorption into the polyimide substrate. Measurements were taken in a faraday cage with a 10 mV AC excitation voltage against open circuit potential and the frequency swept from 100 Hz to 1 MHz.

2.4.2 Cross-talk Results

The impedance sweep of multiple electrode traces from the multi-scale array is shown in the bode plot in Figure 7A, with all curves representing a specific trace based on distance from the reference trace. The impedance magnitude increases as the distance between the reference electrode to the working electrode increases (red trace denotes nearest trace to the reference trace and green trace denotes the furthest trace

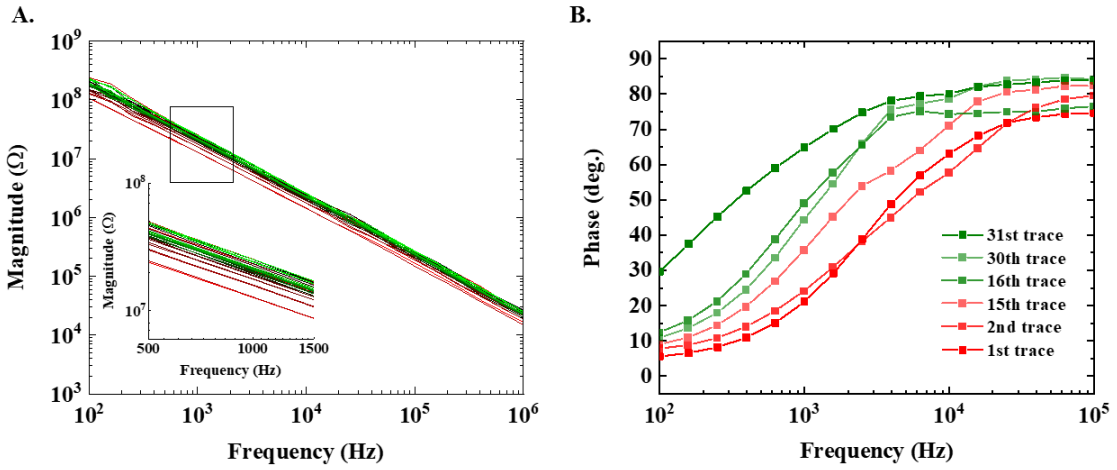

Figure 7. Cross-talk EIS: A. Bode plot representing the impedance magnitude sweep of all 32 traces of the multi-scale array using the macro trace as counter. Red to green indicates an increasing distance between the working and counter trace. B. Bode plot representative of the impedance phase sweep.

from the reference trace) with an average value of 24.5 ±1.2 MΩ at 1 kHz. Figure 7B shows the results of the impedance phase sweep. Only 6 of the 31 traces were shown to clearly visualize the difference in phase from traces that are nearest and furthest from the counter trace. Nearby traces exhibited a resistive component up until 10 kHz in the phase diagram while further traces exhibited a more capacitive behavior (90°) before 1 kHz.

2.4.3 Cross-talk Conclusion

Based on the experiments carried out, cross-talk between neighboring electrodes is insignificant due to the low electrochemical impedance of the electrodes relative to the impedance of the parasitic capacitance between neighboring electrode traces. Considering that the only immersed portions of the array were the electrode body,

future iterations of this experiment can include arrays that have not yet been fully etched to expose the electrodes (completely insulated). This would allow the array to be completely submerged in solution. Further experimentation can also be conducted to specifically investigate the effect that various electrode geometries and sizes have on nearby electrodes based on the embedded geometry as showcased in the multi-scale array.

Chapter 3

DEVELOPMENT OF A NOVEL, CONCENTRIC MICRO-ECOG ARRAY ENABLING SIMULTANEOUS DETECTION FROM MULTIPLE ELECTRODE SIZES

Objective. Detection of the epileptogenic zone is critical, especially for patients with drug-resistant epilepsy. Accurately mapping cortical regions exhibiting high activity during spontaneous seizure events while detecting neural activity up to 500 Hz can assist clinicians' surgical decisions and improve patient outcomes. *Approach.* We designed, fabricated, and tested a novel hybrid, multi-scale micro-electrocorticography (micro-ECoG) array with a unique embedded configuration. This array was compared to a commercially available microelectrode array (Neuronexus) for recording neural activity in rodent sensory cortex elicited by somatosensory evoked potentials and pilocarpine-induced seizures. *Main results* Somatosensory evoked potentials (SSEP) and spatial maps recorded by the multi-scale array ("micros", "mesos", and "macros" referring to the relative electrode sizes, 40 micron, 1 mm, and 4 mm respectively) were comparable to the Neuronexus array. The SSEPs recorded with the micros had higher peak amplitudes and greater signal power than those recorded by the larger mesos and macro. Seizure onset events and high-frequency oscillations ($\sim$450 Hz) were detected on the multi-scale array, similar to the commercially available array. The micros had greater signal to noise ratio than the mesos and macro over the 5-1000 Hz frequency range during seizure monitoring. During cortical stimulation experimentation, the mesos successfully elicited motor effects. *Significance.* Previous studies have compared macro- and microelectrodes for localizing seizure activity in

adjacent regions. The multi-scale design validated here is the first to simultaneously measure macro- and microelectrode signals from the same overlapping cortical area. This enables direct comparison of microelectrode recordings to the macroelectrode recordings used in standard neurosurgical practice. Previous studies have also shown that cortical regions generating high-frequency oscillations are at an increased risk for becoming epileptogenic zones. More accurate mapping of these areas may improve surgical outcomes for epilepsy patients.

3.1 Introduction

The development and evolution of brain-machine interfaces (BMIs) capable of providing high-fidelity information on neurological signals has significantly improved the diagnosis and treatment of neurological disorders. Epilepsy has been at the forefront of neurological research, including the ability to reliably detecting seizure events (Tiwari et al. 2019). Patients with epilepsy make up nearly 1% of the world's population, and of that, roughly 30% fall under the drug-resistant category despite the advances in anti-seizure medication (Englot and Chang 2014; Chen et al. 2018). Surgical resection has been viewed as one of the more effective options for patients with drug-resistant, focal epilepsy even though it is typically only effective in providing patients with long-term seizure freedom 50% of the time (Malmgren and Edelvik 2017; Landazuri et al. 2020). Inherent risks of surgical intervention include complications during surgery, the unnecessary removal of neural tissue, and the risk of recurrence. While neuromodulation therapies have been approved as alternatives to medication and anti-seizure medication, such as vagus nerve stimulation (VNS), deep brain

stimulation (DBS), and closed-loop responsive neurostimulation (RNS), they have provided temporary relief but seldom long-lasting freedom (Ryvlin et al. 2021).

For surgical resection or laser ablation to be effective, proper detection and targeting of the epileptogenic zone (EZ), or brain region responsible for generating seizures, is necessary (Jehi 2018). While non-invasive tools exist including scalp electroencephalography (EEG) and magnetic resonance imaging (MRI), intracranial EEG (iEEG) provides higher resolution and is the gold standard for determining resection. Our work focuses on understanding tradeoffs in iEEG arrays which can be used for stereo encephalography (sEEG), and electrocorticography (ECoG) depending on the depth of the target region (Hasegawa 2016). Implantable probes such as thin-film polymer-based microelectrode arrays (MEAs) have enabled high resolution recording intracranially during seizures. However, these MEAs can cause severe lesions of the target tissue, so advances in the design and development of minimally invasive micro-ECoG arrays are needed (Li et al. 2021; Vomero et al. 2020; Shokoueinejad et al. 2019; Lee et al. 2023). Biocompatibility, flexibility, and conductivity are the primary design considerations for thin-film MEAs. A mechanical mismatch between the surrounding neural tissue and the implantable device is one of the leading causes of device failure and poor recording efficacy, so polymers with low Young's modulus are used to fabricate thin-film MEAs are polyimide (PI), parylene-C, and polydimethylsiloxane (PDMS) with low Young's modulus (stiffness). These considerations led to our design of an iEEG array fabricated on a PI substrate.

Traditional monitoring of epileptic activity was typically focused over the Berger bands (1-25 Hz) using widely spaced clinical macro-sized electrodes. However, studies exploring the power spectral density (PSD) of neural activity in the higher frequency ranges of gamma (25-80 Hz), ripple (80-200 Hz), and fast ripple (>250 Hz) have

shown these frequencies also show features of epileptic activity (G. A. Worrell et al. 2008; G. Worrell et al. 2012; Park and Hong 2019; Schönberger et al. 2020). Recordings from micro-ECoG arrays on epileptic patients have shown that spatially localized epileptiform activity at higher frequencies provide helpful information that macro electrodes are incapable of recording. The combination of traditional multi-millimeter electrodes and microelectrodes on a single array, called hybrid electrode arrays, demonstrated this advantage (Van Gompel et al. 2008; Stead et al. 2010). Hybrid arrays enabled the detection of micro seizures on the microelectrodes, potential interictal biomarkers of epileptic tissue. The concentric array was specifically designed to explore the localization of focal seizures is possible through the combined abilities of multi-scale electrodes within the same recording space.

In this work, we leveraged the properties of micro-ECoG electrode arrays and the hybrid array concepts described previously to develop a novel 32-channel, multi-scale micro-ECoG electrode array. The 32-channel multi-scale concept incorporated three electrode sizes (40 µm, 1 mm, and 4 mm) in a novel concentric design where we carried out *in vitro* tests and *in vivo* recordings of evoked potentials over the somatosensory cortex while also detecting clinical and micro seizure activity. Our objectives were to assess if this novel design was capable of spatially mapping neural activity compared to a gold standard commercial micro-ECoG array (Neuronexus Technologies) and the tradeoffs between the three electrode sizes in localization of neural activity and frequency response. This was achieved by recording somatosensory evoked potentials (SSEPs) and pilocarpine-induced seizure events on a gold standard MEA and our concentric multi-scale array. We analyzed and compared the recordings in both cases for the three electrode sizes and the gold standard to compare localization, frequency response, and signal-to-noise ratio (SNR).

3.2 Materials and Methods

3.2.1 Design of multi-scale array

Electrode geometries for the concentric multi-scale micro-ECoG array (Fig. 8A) include electrode sizes similar to existing clinical standard electrodes in order to directly compare with conventional devices. The 4 mm macro and 40 µm micros correlate to the typical diameters of subdural grid electrodes and strips as well as platinum microwires. The 1 mm mesos were intended to mimic typical penetrating electrodes that have 1 mm diameters. The macro and meso electrode sizes can also be used to stimulate. Based on G. Worrell et al. (2012), center-to-center electrode spacing is 350 µm for the micros and 1.5 mm for mesos. The concentric configuration has high electrode density with limited connections while maintaining spatial detail. In total, the multi-scale array is composed of 1 macroelectrode, 4 mesoelectrodes, and 27 microelectrodes (Fig. 8C).

A polyimide substrate is thin and highly flexible with a simple manufacturing process. Polyimide is a widely used material for creating flexible printed circuit boards (PCBs) (Lenihan et al. 1996; Engel, Chen, and Liu 2003; Dobrzynska and Gijs 2012). A spin-coated polyimide variant, PI-2611 (HD Microsystems, Parlin, NJ, USA), was used to create a 10 µm substrate layer and 10 µm insulation layer for a total thickness of 20 µm maintaining the array's flexibility. Electrodes were created by depositing 5 nm of titanium (Ti) and 100 nm of platinum (Pt), which enabled a stable charge density and ensured biocompatibility for neural recording and stimulation. Figure 8B highlights the fabrication process. Metal adhesion was confirmed with an ASTM D3359 tape test. Contacts were exposed by dry etching PI-2611 with oxygen plasma

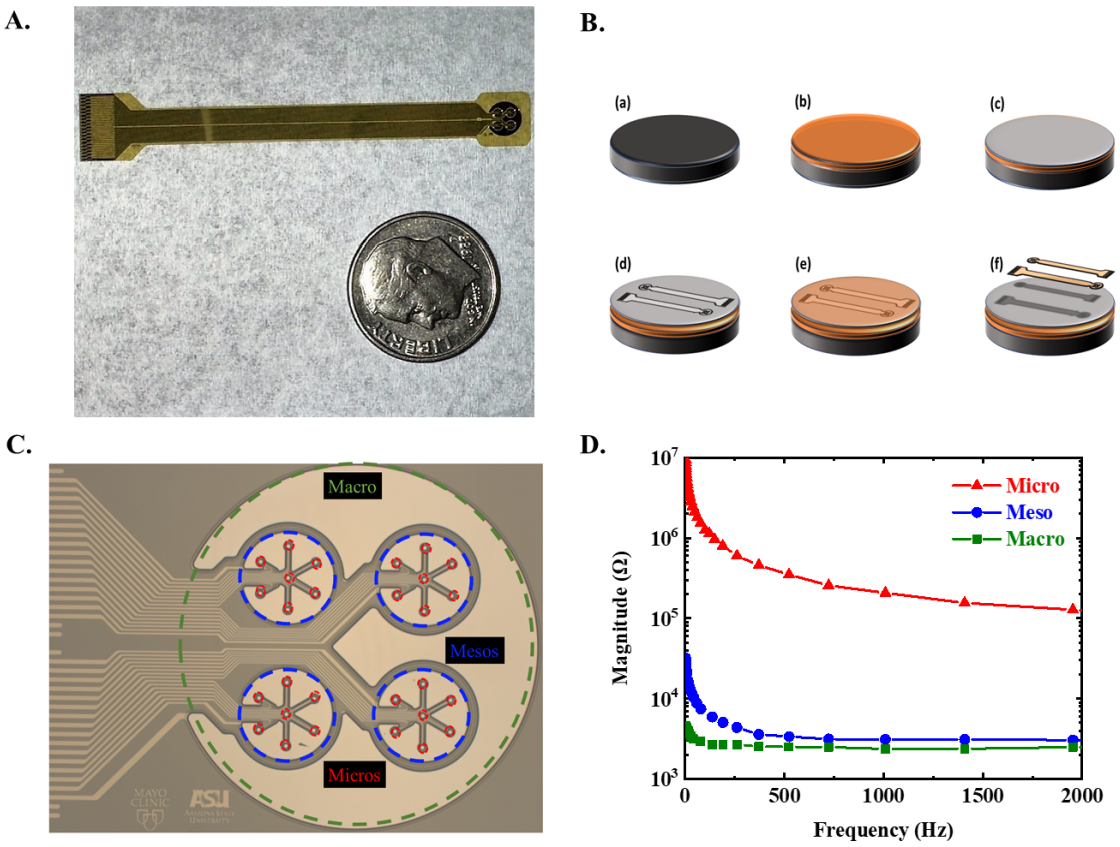

Figure 8. 32-channel multi-scale array. A. Picture of array after release from wafer. B. Protocol used to fabricate multi-scale array: (a) silicon wafer; (b) spin polyimide; (c) metal layer deposition; (d) patterning; (e) insulation layer deposition and spin photoresist; (f) pattern, etch and removal of photoresist and release from silicon wafer. C. Microscope image of 32-channel multi-scale array with electrodes highlighted (micros: red, mesos: blue, and macro: green). D. Electrochemical impedance spectroscopy (EIS) magnitude plot of micros, mesos, and macro.

to prevent biotoxicity. Pieces of 127 µm thickness polyether ether ketone (PEEK) were applied as backing to insert the array into a 39-pin zero insertion force (ZIF) connector. A custom electrode interface board (EIB) design enabled connection from the ZIF connector to an Intan RHD electrophysiology evaluation system (Intan Technologies, Los Angeles, California, USA) through Omnetics connectors (Omnetics Corporation, Minneapolis, MN, USA). Additional EIB designs were created to interface the multi-

scale array and benchtop characterization equipment. All connections were confirmed with multimeter probes before use. All fabrication was performed at Arizona State University, with work being completed in the ASU Nanofab (Class 100) and soft lithography lab (Class 1000) cleanrooms.

3.2.2 Benchtop Characterization

Potentiostatic electrochemical impedance spectroscopy (EIS) was performed in 1x phosphate buffer saline (PBS) at room temperature with a SquidStat Plus Potentiostat (Admiral Instruments, Tempe, AZ, USA). A Ag/AgCl electrode suspended in 3M NaCl solution and a 23 cm long platinum coil (BASi Research, West Lafayette, IN, USA) were used to complete the three-electrode cell setup. Frequency was swept from 1 Hz to 1 MHz with a 10 mv RMS AC source and 0.5 V DC offset. Complex impedance data was converted, averaged, and plotted in MATLAB.

3.2.3 Arrays & implantation

Two arrays were used in this experiment, the described multi-scale array and a NeuroNexus (NNx) 32-channel micro-ECoG array (Neuronexus Technologies, Ann Arbor, MI, USA). Fig. 9A shows a magnified image of the recording area of both arrays. The NNx micro-ECoG array consisted of a 15 µm thin polyimide substrate, 3.6 x 3.6 mm area with 32 platinum contacts (100 µm diameter). The contacts were arranged in a grid with 600 µm interconnect distances. Animal studies were conducted following ethical guidelines set by the United States National Institutes of Health and

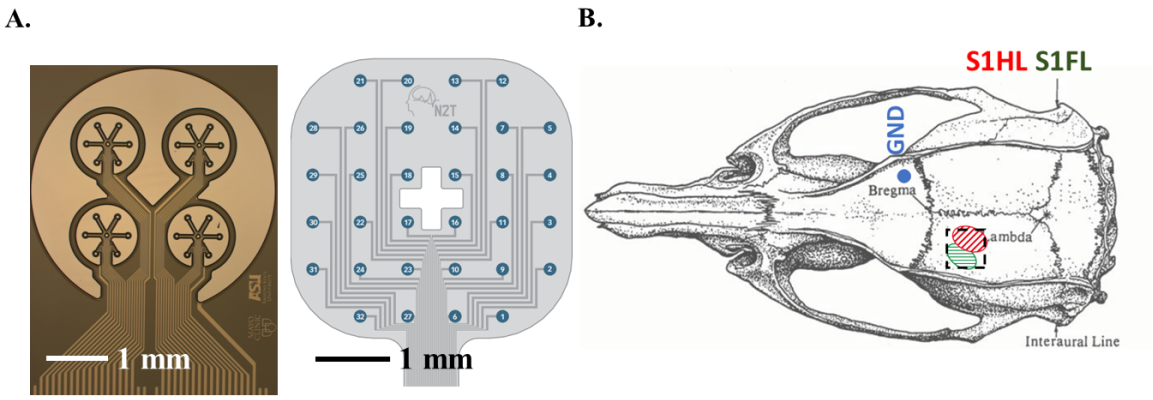

Figure 9. Multi-scale and Neuronexus arrays. A. Magnified image of the multi-scale and Neuronexus arrays detailing the electrodes. B. Placement location of the arrays over the somatosensory cortex; S1HL: hindlimb, S1FL: forelimb.

the specific protocol 21-1822R approved by the Institutional Animal Care and Use Committee at Arizona State University.

3.2.4 Recording of somatosensory evoked potentials

Three (two male, one female) Sprague-Dawley rats (250-350g) were used in gathering SSEP data. To prepare for measurements, rats were placed in a stereotactic apparatus and anesthetized using an initial dose of 5% isoflurane and then maintained under anesthesia with a mix of 2% isoflurane and continuous oxygen flowing at 2 liters per minute (lpm) delivered through a nose cone. Vitals were monitored with a MouseOx Plus pulse oximeter (Starr Life Sciences Corporation, Oakmont, PA, USA), and internal temperature was maintained with a heating pad and towels and monitored by a rectal probe. A single 5 mm x 10 mm window craniotomy was performed over the left hemisphere (coordinates with respect to bregma; 7 mm posterior, 3 mm anterior, 5.5 mm lateral, 0.5 mm medial). Before stimulation, sites were shaved and cleaned with disinfectant. A similar approach to previous studies was taken in the gathering

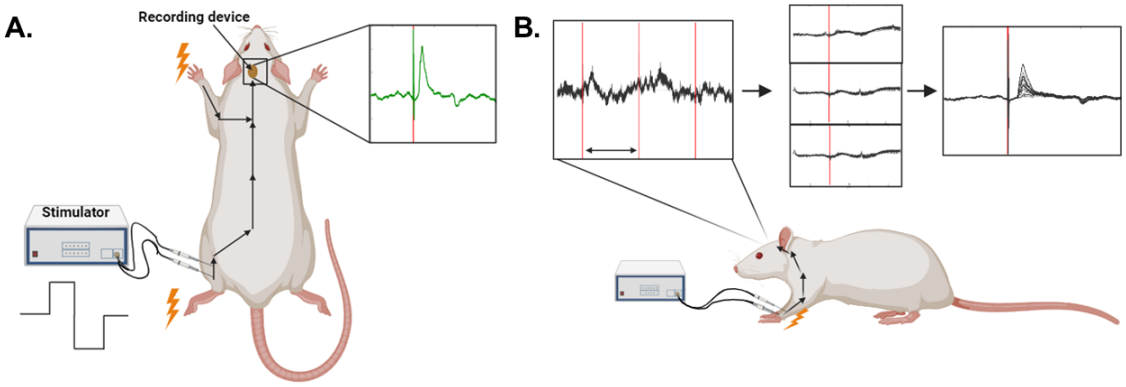

Figure 10. SSEP experimental setup. A. Overview of the experimental SSEP setup indicating the stimulation, signal pathway, and expected recorded signal. B. SSEP recording overview highlighting the transition from the recording of the raw signal, followed by transposing the raw signal into 1 second windows, and lastly averaging those windows to create the final SSEP trace.

and processing of SSEP data (Hosp et al. 2008; Moncion et al. 2022). Constant current pulses (1 Hz, 0.5 mA, 2 ms duration) were delivered via bipolar needle electrodes to the median and tibialis nerves (A-M Systems, Sequim, WA, USA). Epidural potentials were amplified through an RHD 2132 32-channel headstage (Intan, Los Angeles, CA, USA), obtained with a 5 kHz sampling rate and filtered (0.72-7000 Hz bandpass). An illustrated schematic showing an overview of the recording setup is shown in Figure 10A.

3.2.5 Pilocarpine-induced epileptic rat model

Four (two male, two female) Sprague-Dawley rats (250-350g) were used as seizure models for this study. Rats were anesthetized using an initial dose of 5% isoflurane and then maintained under anesthesia with a mix of 2% isoflurane and continuous oxygen flowing at 2 liters per minute (lpm) through a nose cone. A double window craniotomy

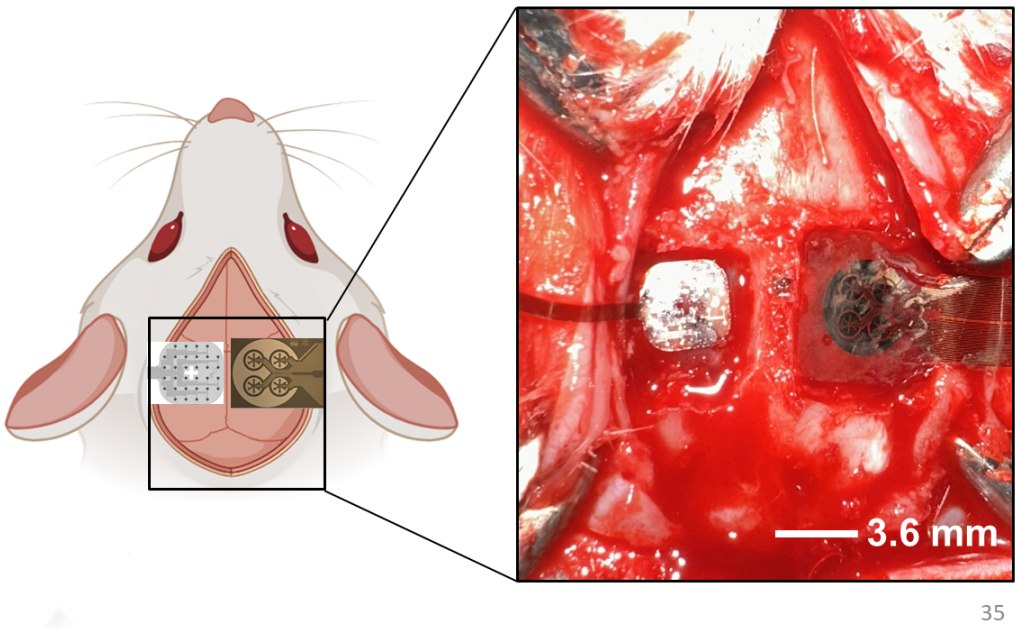

Figure 11. Diagram indicating the double craniotomy and placement of the multi-scale and NNx arrays (left) with actual image from one surgery (right).

was performed, with each window being 5 mm x 7 mm (Figure 11). Baseline neural signals were recorded for 5 minutes to determine regular activity. Following baseline recording, 300 mg/kg of pilocarpine hydrochloride (Sigma Aldrich, St. Louis, MO, USA) was injected intraperitoneally following similar procedures to previous studies (Curia et al. 2008; Turski et al. 1983). Neural signals were recorded with a 5 kHz sampling frequency using two RHD 2132 32-channel headstages. Intracranial recording commenced, and we maintained visual observation of potential seizure symptoms.

3.2.6 Cortical Stimulation Evaluation

Two (one male, one female) Sprague-Dawley rats (250-350g) were used. Instead of isoflurane, a ketamine-xylazine anesthetic was chosen to preserve motor nerve

function. Before the craniotomy, anesthesia was induced using the ketamine / xylazine (KX) cocktail with a dose of (75/10 mg/kg) through intraperitoneal (IP) injection. Anesthesia was maintained using a ketamine dose of 25 mg/kg administered every 45 to 60 minutes and a xylazine dose of 5 mg/kg every 2 hours. Anesthesia was verified by squeezing the rat's foot pad every 15 minutes to confirm the loss of withdrawal response. A window craniotomy was performed 4 mm posterior to lambda and 4 mm anterior to bregma, and 4 mm lateral from midline for an entire 4 mm x 12 mm window. A 200 µm stainless steel wire was placed under the scalp as a reference wire. Cortical stimulation was performed across two meso electrode configurations (between electrodes m2 and m16 and between electrodes m16 and m17, as shown by the red and green double arrows) shown in Fig. 12. Placement 1 and placement 2 depict the two locations on the cortical surface that were stimulated using an isolated pulse stimulator (Model 2100, A-M Systems, Sequim, WA, USA). Biphasic pulses were set with a width of 200 µs, a 10 ms inter-stimulation interval, and a 100 ms train duration with 1 sec between trains. Stimulation amplitude was incrementally increased until a motor response was evoked (or the 4 mA limit was reached) to obtain a minimal cortical activation threshold. Two separate stimulation locations on the cortex, separated by 2 mm, were used during the placement of the electrode array to attempt to stimulate both the hindlimb and forelimb of the rodent.

3.2.7 Signal Analysis

Data analysis was completed using MatLab (Version 7, The MathWorks Inc., Natick, MA, USA). Somatosensory traces were obtained from the raw recorded waveforms by segmenting the 3 minutes of recorded data into 180 individual windows, transposing

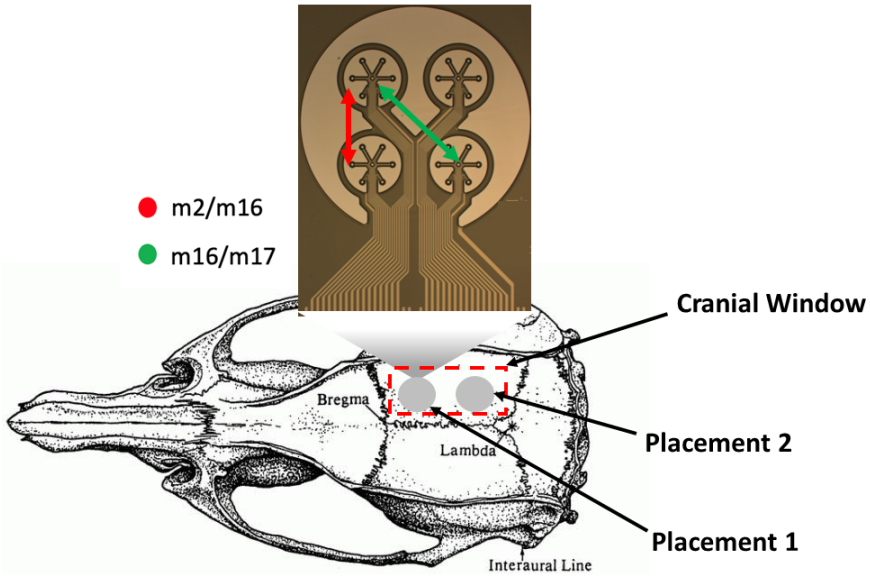

Figure 12. Schematic of multi-scale array placements for cortical stimulation. Placements 1 and 2 depict the two array placements during the cortical stimulation and are located approximately 2 mm apart. The m2/m16 and m16/m17 arrows highlight the stimulation direction for each stimulation pair.

those windows and then averaging all 180 windows (Figure 10B). Further SSEP processing was performed using the MatLab toolbox BrainStorm (Tadel et al. 2011). Recorded evoked potentials were filtered with a 60 Hz notch filter and segmented into -100 to 200 ms epochs in reference to the stimulation (0 ms). Averaged epochs were used to compute common SSEP characteristic's latency and full-width half maximum (FWHM). BrainStorm and Origin 2018 (OriginLab, Northampton, MA, USA) were used to analyze and plot the recorded data from pilocarpine-induced seizure models. To quantify the performance of the different electrode sizes, we computed the signal-to-noise ratio (SNR) of each electrode. SNR is conventionally found by taking the ratio of the mean peak-to-peak amplitude of the signal with respect to the mean standard deviation (SD) of the baseline activity. This method of SNR quantification is referred

to as the voltage SNR, or vSNR and is broadly used when there is not a need for the full information provided by spectral analysis (Blaschke et al. 2017). However, because the signals of interest have frequency dependent information encoded, we computed the spectral SNR. Spectral SNR was computed as the ratio of the power spectral density (PSD) during the active state (Up state) with respect to the power during the resting state (Down state) (Suarez-Perez et al. 2018). In this study, we investigated the spectral SNR of the micro, meso, and macro electrodes on the multi-scale array to determine the recording efficacy of the varying electrode sizes at different relevant frequencies.

3.3 Results

3.3.1 Electrochemical Impedance Spectroscopy

Complex impedances were measured from 54 micros, 8 mesos, and 2 macro electrodes on the multi-scale array (2 arrays) and all 32 electrodes from the NNx array. The measurements were consistent throughout the recordings. Impedances shown in Fig. 8D were as expected for electrode geometries on the multi-scale array; lower impedances for larger electrodes and higher impedances for smaller electrodes. The impedance magnitudes at 1 kHz were: 3.2 ± 0.2 kΩ for the macros, 4.4 ± 0.4 kΩ for the mesos, 212.2 ± 20.4 kΩ for the micros, and 105.5 ± 12.3 kΩ for the NNx electrodes.

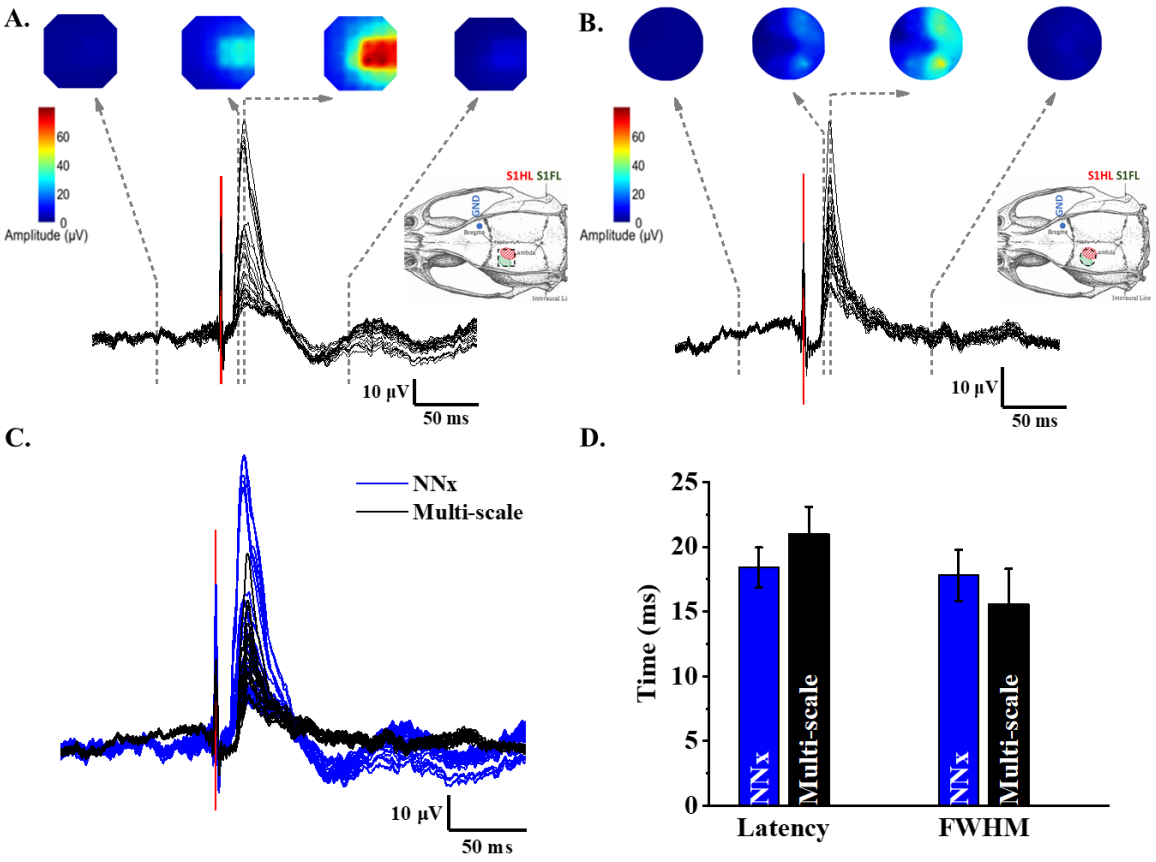

Figure 13. Somatosensory evoked activity from hindlimb (HL) stimulation. A. SSEP activity traces from all 32 electrodes on the NNx array with the red line indicating the stimulation point. Heat map showing the spatial distribution of SSEP activity corresponding to the NNx array layout shown in the inset for each time point denoted by the dashed gray line. B. SSEP activity traces from the 22 working micros from the multi-scale array. Heat map showing the spatial distribution of SSEP activity corresponding to the layout shown in the inset for each time point denoted by the dashed gray line. C. SSEP traces from 32 electrodes on NNx overlayed with 22 micros from multi-scale array. D. Bar chart comparing SSEP latency and FWHM from the average of the traces from each array.

3.3.2 Somatosensory evoked activity recording

Somatosensory evoked potentials were selected for *in vivo* experiments because they are widely accepted as highly repeatable allowing for direct comparison of spatial

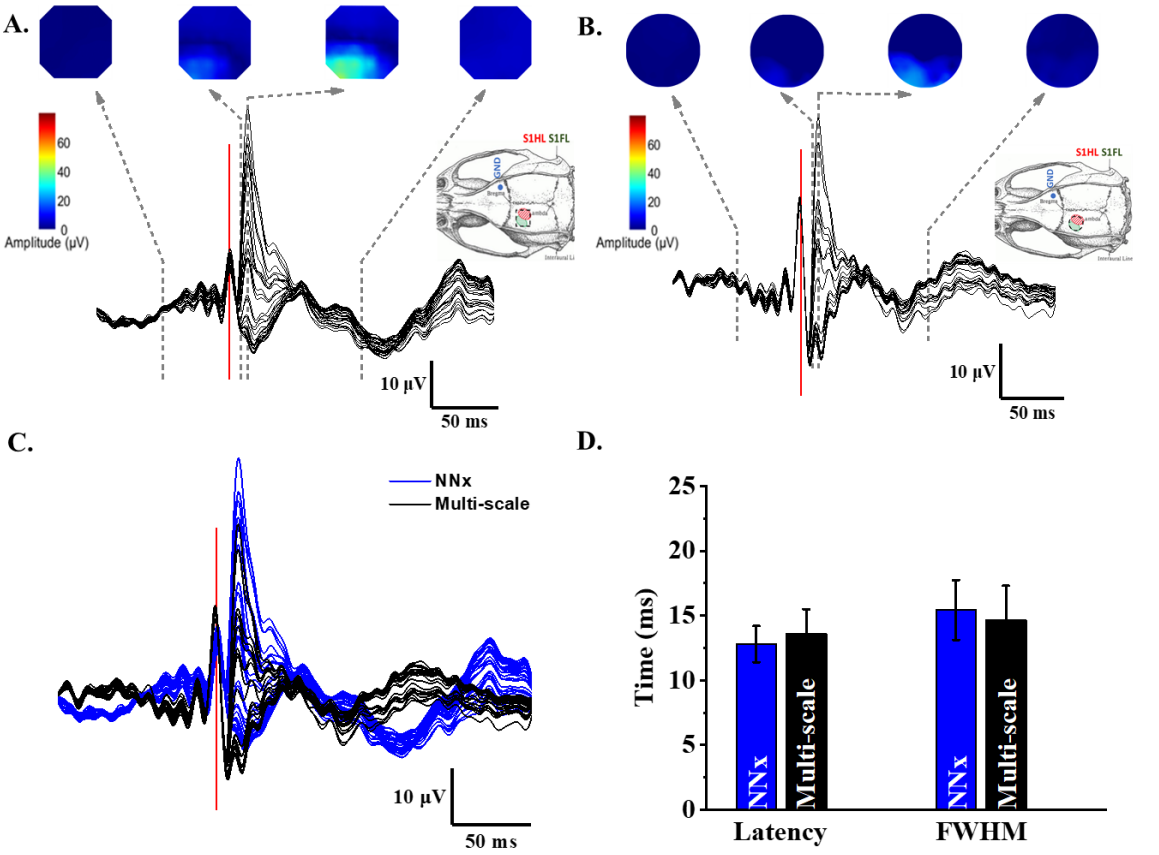

Figure 14. Somatosensory evoked activity from forelimb (FL) stimulation. A. SSEP activity traces from all 32 electrodes on the NNx array with the red line indicating the stimulation point. Heat map showing the spatial distribution of SSEP activity corresponding to the NNx array layout shown in the inset for each time point denoted by the dashed gray line. B. SSEP activity traces from the 22 micros from the multi-scale array. Heat map showing the spatial distribution of SSEP activity corresponding to the layout shown in the inset for each time point denoted by the dashed gray line. C. SSEP traces from 32 electrodes on NNx overlayed with 22 micros from multi-scale array. D. Bar chart comparing SSEP latency and FWHM from the average of the traces from each array.

resolution between our multi-scale array and the NNx array. The SSEPs have a distinct time-locked waveform for a given site-specific stimulus. The recorded evoked potentials were averaged over multiple stimuli events to create an average waveform representative of the elicited activity.

In this study, we monitored evoked responses from hindlimb (HL) and forelimb (FL) stimulation. Fig. 13A shows the response measured from the HL stimulation, and 13B shows the response measured from the forelimb (FL) stimulation for the NNx and multi-scale arrays. Above each SSEP trace is a heat map showing the spatial distribution of the evoked activity at varying time points along the SSEP trace to determine localization. The HL heat map shows more pronounced localization than the FL heat map, which we attribute to the array placement being more centered over the S1 HL region of the cortex. Although the electrode sizes from both arrays allow for spatial distribution, the overall array size does not allow for full coverage of the S1 region of the cortex. Figs. 13C and 14C highlight the differences between the recorded signal from the electrodes on the NNx array and the micro electrodes from the multi-scale array, as a means to compare the most similarly sized electrodes. Most traces on the NNx array appear to have greater peak amplitudes than the peaks of the multi-scale array, which we ascribe to the larger electrode size of the NNx array (100 µm) compared to the micros on the multi-scale array (40 µm). Average latency and FWHM were plotted in Figs. 13D and 14D for both arrays. The NNx SSEP HL stimulation had an average peak latency of 18.40 $\pm$1.56 ms and FWHM of 17.89 $\pm$1.98 ms (Fig. 13D). The corresponding values for the multi-scale array were 21.11 $\pm$2.11 ms and 15.66 $\pm$2.72 ms (Fig. 13D). Results obtained from both arrays for HL SSEP were highly consistent. The FL SSEP recordings for the NNx array resulted in an average peak latency and FWHM of 12.82 $\pm$1.44 ms and 15.43 $\pm$2.31 ms, respectively. The corresponding values for the multi-scale array were 13.63 $\pm$1.95 ms and 14.65 $\pm$2.65 ms (Fig. 14D). Analysis using the non-parametric Mann-Whitney test ($p<0.05$) revealed that none of the values between the multi-scale array and NNx array were statistically significant

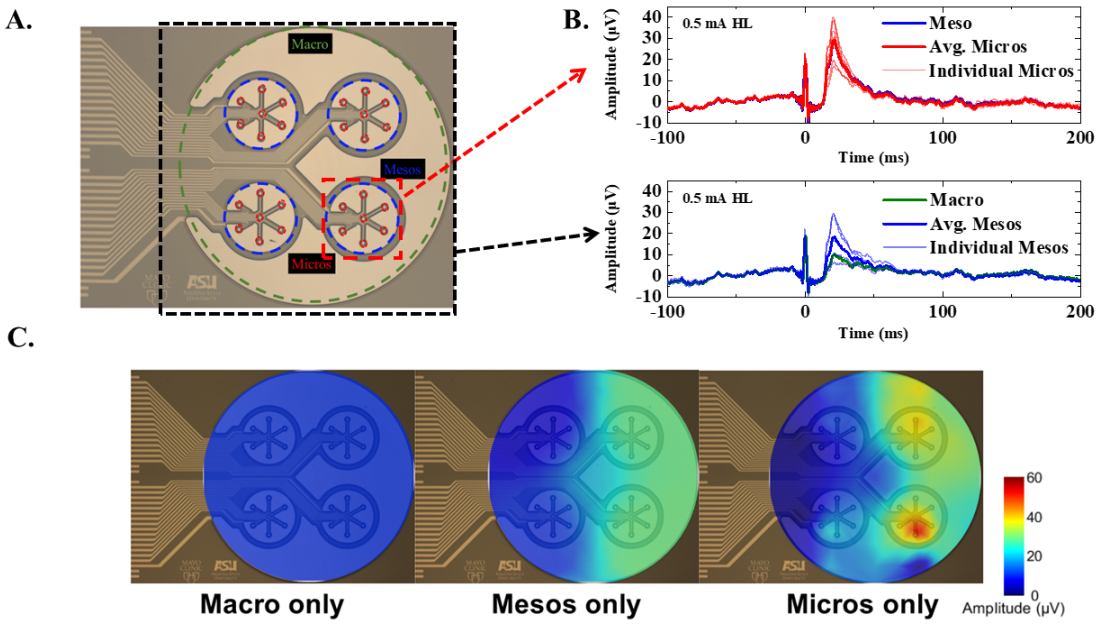

Figure 15. Somatosensory evoked activity from hindlimb (HL) stimulation. A. Magnified image of multi-scale array highlighting the specific electrodes that are analyzed in B. B. *Top:* Data from a quadrant of electrodes (red box) that compares the average recorded activity of the micros (red) in that quadrant to the recorded activity of the meso (blue) from 0.5 mA HL stimulation. *Bottom:* Data from 0.5 mA HL stimulation comparing the average recorded activity of the four mesos (blue) to the recorded activity of the macro (green). C. Heat map indicating the spatial resolution from HL stimulation from *left:* the macro electrode only, *middle:* the four meso electrodes only and *right:* the micro electrodes only.

To examine the recording capability of the different electrode sizes, a deeper analysis of the recorded traces from the micro, meso, and macro electrodes were investigated from the HL stimulation. Fig.15A indicates which set of electrodes are analyzed in 15B. The average of the micro electrodes in the quadrant boxed in red are compared to the meso electrode from that same quadrant. The average of the micro traces had a peak amplitude of 29.18 ±3.24 μV and a peak latency of 20.8 ±1.2 ms. The meso electrode from that same quadrant had a peak amplitude of 28.33 ±1.26 μV and peak latency of 21.4 ±0.76 ms. The bottom plot in Fig.15B highlights the

average traces of the meso electrodes compared to the activity trace of the macro electrode from the same HL stimulation. The averaged mesos had a peak amplitude of 18.36 ±4.34 µV and peak latency of 21.2 ±0.95 ms, while the macro had a peak amplitude of 11.65 ±1.87 µV and peak latency of 21.4 ±0.34 ms. Fig.15C illustrates the difference in spatial mapping when only the four meso electrodes are used (left) and when only the 27 micro electrodes are used (right). The heat map from the micro only distribution clearly showed an improved spatial resolution of the high activity localization when compared to the meso only heat map.

We have demonstrated that the hybrid, multi-scale array can record neuronal modulation and performs comparably to a commercially available micro-ECoG array. The performance of the micro, meso, and macro electrodes were compared to one another during the SSEP validation and results clearly were indicative that the micros had greater signal power and localization of the evoked activity on the cortex when compared to the meso and macro electrodes.

3.3.3 Seizure model

Epileptiform discharges and seizure propagation were simultaneously monitored on both hemispheres by completing a double craniotomy and placing the multi-scale micro-ECoG array on one hemisphere and the NNx on the other. The arrays are centered over the same locations, covering multiple cortical regions on each hemisphere. Fig. 16 shows selected examples of seizure events recorded from both arrays. Fig. 16A depicts the transition from a normal, non-epileptic state to a seizure state from the multi-scale array. Cortical electrophysiological activity intensifies significantly during the seizure onset. The peak-to-peak potentials during the baseline state were 99.23

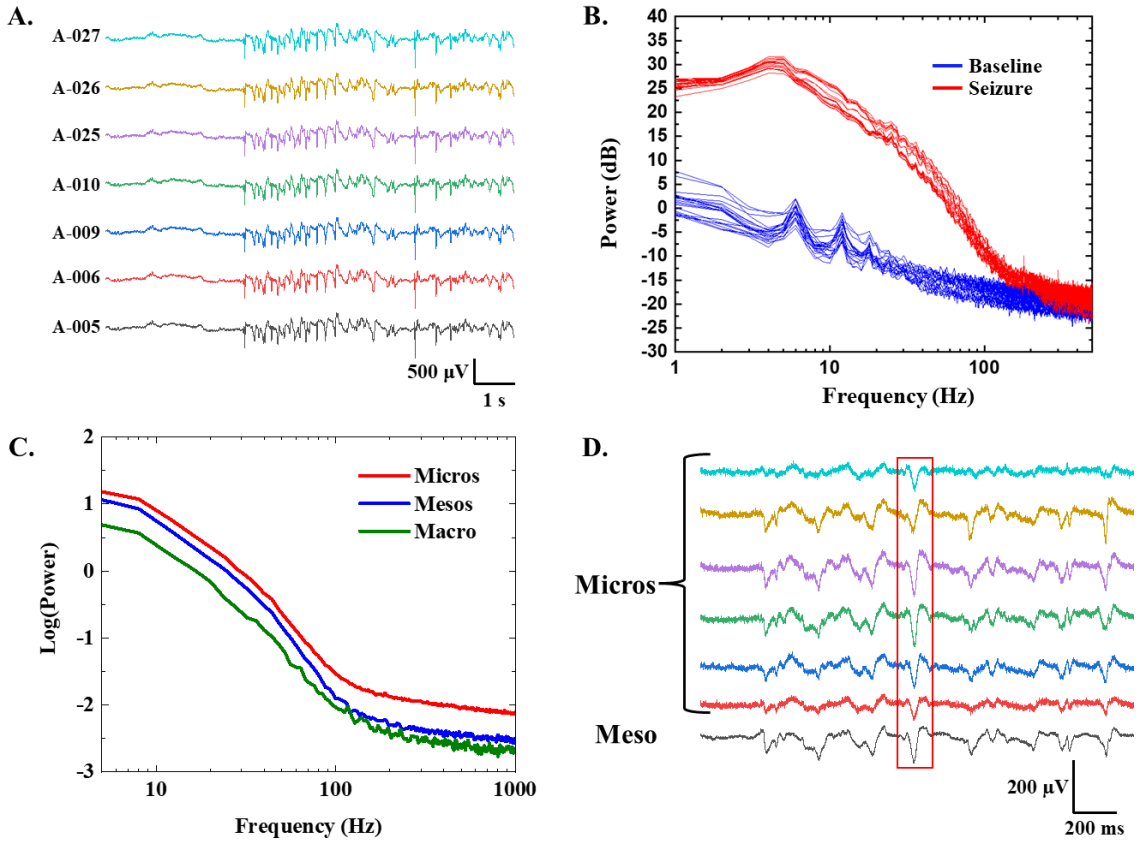

Figure 16. Epileptic events recorded from multi-scale array. A. ECoG signal change recorded on an example subset of electrodes on the multi-scale array during a transition from baseline to seizure status. B. Power spectral density comparing the baseline and seizure status. C. Average power spectra of the micros, mesos, and macro from 5-1000 Hz during the seizure state. D. Example of an interictal seizure spike (red rectangle) from the micros and meso from the same quadrant on the multi-scale array.

± 1.09 µV and increased to 492.17 ± 7.01 µV during the seizure state. The power spectral density (PSD) for all 32 electrodes on the multi-scale array was calculated during baseline and seizure status (Fig. 16B). The PSD curves exhibited the greatest concentration of power in the 1-30 Hz region, with the curves during the seizure status showing higher power than during the baseline phase. Significant peaks occurred in the 5-7 Hz theta frequency band, a hallmark of seizure activity. Studies show that

change in theta band power may be a biomarker for potential epileptogenesis. As shown in the HL SSEP analysis, the micros clearly showed improved signal power over a large frequency range (5-1000 Hz) when compared tp the meso and macro electrodes during the seizure state (Fig.16C). The quadrant of electrodes discussed in Fig.15A are illustrated again in Fig.16D and show a recorded interictal spike (red rectangle). The example of this interictal spike shows the difference in amplitude between similarly located micros and their respective meso electrode.

The microelectrodes on the multi-scale array were also capable of recording high-frequency oscillations (HFOs), as expected due to the appropriately small size of the recording electrodes (< 100 µm). Fig. 17A and B show an example of a 450 Hz signal recorded from both arrays depicting the asynchronous and spatially diverse nature of the recorded HFO across non-adjacent microelectrodes. The shaded lines in Fig. 17C depict the recorded signal from each individual electrode on the multi-scale array, while the bolded line depicts the average for each respective electrode geometrical size (micro, meso, macro) for the recorded HFO segment highlighted in Fig. 17B. The spectrogram in Fig. 17D shows the time segment of the recorded HFO from a micro (top), meso (middle), and macro (bottom) electrode and clearly highlights the diminishing strength of the HFO as the size of the recording electrode increased.

3.3.4 Spectral SNR

Electrode SNR is dependent on electrode impedance and thus is frequency-dependent. Because of this, quantitatively evaluating SNR at different biological frequencies is essential in characterizing electrode performance. Spectral SNR was evaluated for each electrode size (micro, meso, and macro) in order to compare them

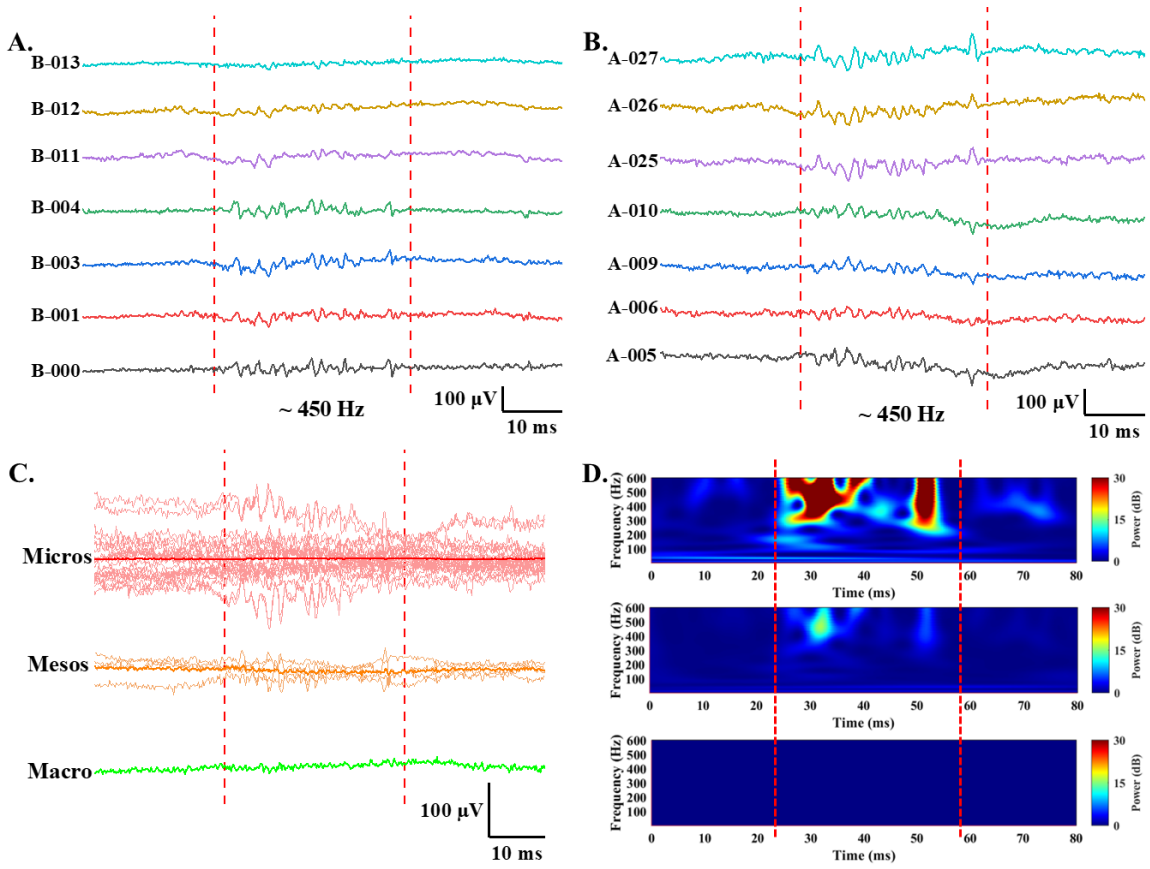

Figure 17. HFO recordings A. HFO recorded from a subset of electrodes on the NNx array. B. Same HFO recorded from a subset of electrodes on the novel multi-scale array. C. Same HFO recording from the plots above; bold traces highlight the average for the micros and mesos, and macro, with thinner lines showing all individual channels. D. Time-frequency power spectrogram, from top to bottom, of an example micro, meso, and macro electrode for the recorded HFO.

over the biologically relevant frequency ranges by calculating the PSD of the Up states (signal) and the Down states (baseline) (Figure 18A). Overall, from the spectral SNR analysis we found that all three electrode sizes had relatively consistent SNR in the low frequency range up to 30 Hz (Figure 18B). At this frequency range, the micro electrodes had an SNR roughly about 17 dB and the meso electrode around 16 dB. The SNR of the macro in this frequency range was significantly lower at about 9 dB. For frequencies greater than 30 Hz, the SNR decayed almost linearly following the

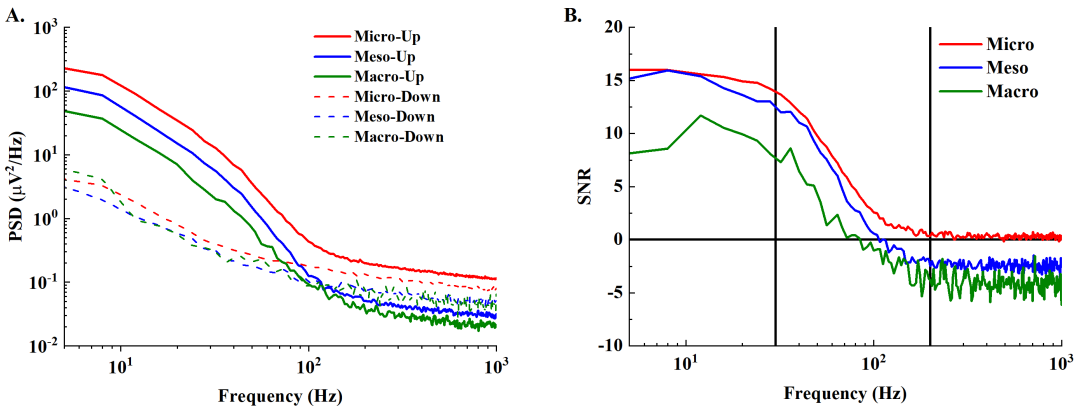

Figure 18. Spectral signal-to-noise ratio (SNR) A. Mean PSD of the normal ("Down", dotted line) and active seizure states ("Up", solid line) for the micro, meso, and macro electrodes. B. SNR was calculated for each frequency in the range of 5-1000 Hz for all three electrodes (micros, mesos, and macro). Horizontal line at 0 SNR demarcates where SNR=0 ($\text{Up}_{PSD} = \text{Down}_{PSD}$). The two vertical lines at f=30 Hz and 200 Hz separate three frequency bands (4-30 Hz = low, 30-200 Hz = medium, and 200-1000 Hz = high).

typical 1/f decay until each electrode hit a plateau at varying frequencies. Throughout the entire frequency spectrum analyzed the electrode SNR was inversely related to the electrode size, meaning the micros had the greatest SNR and the macros had the smallest. These results corroborated what was seen in the SSEP analysis (Figure 16D). The micro electrodes were the only electrode size to have positive SNR throughout the entire low and medium frequency ranges and eventually plateaued at 0 dB past 700 Hz while the meso and macro electrodes eventually reached negative SNR past 100 Hz and 85 Hz respectively. Negative SNR at the higher frequencies were caused because the Down PSD states exceeded the Up PSD states. This effect may be caused by some noise artifact. As expected, the recording performance of the electrodes diminished at higher frequencies, with the micros performing best.

Table 2. Cortical stimulation from multi-scale array.

Pair	Placement	Threshold (mA)	Movement Observed	Source Distance (mm)
m2/m16	1	3.2	Whisker/Forepaw	1.5
m2/m16	2	3.6	Forepaw/Jaw	1.5
m17/m16	1	2.6	Forepaw	2.12
m17/m16	2	2.4	Hindpaw	2.12

3.3.5 Cortical Stimulation

Stimulus pulse widths of 100 µs were tested but did not produce successful motor effect, so 200 µs pulses were used instead. Table 2 reports the minimal cortical threshold current (in mA) required to elicit an observable movement from the two separate array placements on the brain. Forelimb activation occurred at a minimum cortical simulation of 2.6 mA between the m16 and m17 meso electrodes. The stimulation between the m2 and m16 meso electrodes, which are laterally aligned, evoked whisker movement and wrist pronation at a stimulus of 3.2 mA.

For additional motor mapping, the multi-scale array was moved 2 mm caudally, and the stimulation patterns were repeated. Hindlimb activation was observed from a 2.4 mA stimulation between the m16 and m17 electrodes. The stimulation between the m2 and m16 electrodes elicited forelimb and jaw movement at a stimulus of 3.6 mA.

3.4 Discussion

In this study, we successfully designed, fabricated, and characterized a flexible, multi-scale, hybrid micro-ECoG array for recording SSEP neural activity and pilocarpine-induced seizure activity. As expected, the electrochemical characterization showed that the impedance magnitudes of the multi-scale array decreased with in-

creasing electrode size. Successful recording and spatial mapping of the hindlimb and forelimb SSEPs highlighted the similarity in spatial resolution between the "micros" on the multi-scale array and the electrodes on the commercially available NNx array. Although the recorded evoked potentials from the micros on the multi-scale were slightly diminished compared to those recorded using the electrodes on the NNx array, we attribute this to the difference in their electrode size. Simultaneous monitoring of the SSEPs from the multiple electrode sizes on the multi-scale array showed that the micros had increased signal power and improved spatial localization of elicited activity over the mesos and macros. Our results also verified what others had hypothesized: SSEP amplitudes were greater when recorded from smaller electrodes (Castagnola et al. 2015).

The model of epilepsy induced by pilocarpine effectively produced electrographic seizures and HFOs that are typical of epileptogenic tissue. These HFOs have been linked to the regions that generate seizures and the development of chronic epileptogenesis, as demonstrated by previous studies (Bragin, Wilson, and Engel 2000; Schönberger et al. 2020). Our study aimed to address the hypothesis put forward by Sindhu et al. (2023), who altered the physical area of an electrode array by shorting neighboring electrodes. We monitored activity simultaneously using multiple electrode sizes in the same location, unlike previous studies that could only sequentially monitor the same area with electrodes of various sizes. Our results showed that microelectrodes were better at recording activity with higher signal power and improved SNR, as measured using spectral SNR analysis. This analysis provided frequency-dependent insights relevant to the neurologically significant frequency ranges. Interestingly, we found that the smallest electrodes (micros) had the highest SNR, while the largest electrode (macro) had the lowest SNR from 5-1000 Hz (Figure 18). Furthermore,

compared to mesos and macro electrodes, micros were significantly more effective at detecting HFOs (Figure 17). These results further shed light on the improved performance of the micro electrodes over the larger meso and macro electrodes.

However, our study had a few limitations. Although the novel concentric design allowed us to monitor the same location with multiple electrode sizes simultaneously, it limited the ability to produce traditional heat maps and compare the spatial resolution against a standard grid array. Additionally, clinical translation of the multi-scale array would require extensive animal testing, long-term studies, and scaled manufacturing capabilities. Multi-electrode arrays with polyimide substrates have been proven successful in long-term animal use when implanted for over six months, with the only issue being dura mater growth encompassing the array (Romanelli et al. 2019). In parallel with developing new bio-materials to prevent bio-fouling of the implanted array, a need for improved *in vitro* and *ex vivo* models before trials move to *in vivo* models would have the potential to reduce the total number of animal models significantly used (Gulino et al. 2019).

This innovative micro-ECoG array is the first of its kind to enable the simultaneous monitoring of multiple electrode sizes from a single location in the brain. By examining neurological phenomena across various electrode sizes, we can gain a better understanding of how electrode size impacts the quality and types of neurological events recorded. For years, clinicians and researchers have been searching for effective ways to localize the epileptogenic region in patients with drug-resistant epilepsy, and the detection of HFOs has emerged as a crucial indicator (Jacobs and Zijlmans 2020). The groundbreaking research of Morrell (2011) has shown that seizures can be significantly reduced through cortical stimulation of predetermined seizure foci. Our multi-scale array design not only allows us to capture brain activity, but also to stimulate it,

providing clinicians with multiple treatment options for patients with drug-resistant epilepsy. By leveraging the multi-scale array to detect HFOs with the micros and then employing the mesos for stimulation, our work paves the way for significant progress in the treatment of drug-resistant epilepsy.

3.5 Conclusion

Our research has successfully analyzed the trade-offs between the multiple electrode sizes of the concentric multi-scale array by monitoring a range of neurological signals elicited from SSEPs and pilocarpine-induced seizures. We have thoroughly investigated the impact of electrode size over equivalent recording areas and found that using a clinically-sized macro electrode does not increase the SNR at lower frequencies as hypothesized. Moreover, our analysis has revealed that using larger electrodes negatively impacts spatial resolution in areas of interest. Our results highlight the unique benefits of high-density micro-electrode arrays, which offer exceptional spatial resolution and superior SNR of neurological signals across clinically relevant frequency ranges. Although minute changes in overall electrode size may have frequency-dependent effects, our data unequivocally show that using uniformly sized micro-electrode arrays is more than sufficient for monitoring neural signals. The experimental analysis performed with the multi-scale array clearly demonstrated that the micro electrodes out performed the larger meso and macro electrodes in SNR and spatial resolution, thus paving the way for future work to focus on using high-density micro-electrode interfaces.

Chapter 4

IN VIVO MULTI-SPECIES CORTICAL MONITORING OF PH CHANGE AND ELECTRICAL ACTIVITY WITH A MODIFIED CONCENTRIC, MULTI-SCALE, MICRO-ECOG ARRAY

Objective. Epilepsy is one of the most common neurological disorders and is characterized by what is often referred to as a "storm of electrical activity". Real-time monitoring approaches have focused on electrical recordings, most commonly from electroencephalography (EEG) and electrocorticography (ECoG) arrays. Herein we demonstrate a novel multi-species approach integrating pH sensitive electrodes and explore its role in monitoring and understanding the relationship pH change has with the electrical activity seen during seizure events. *Approach.* Using a concentric multi-scale array, we modified a 1 mm diameter "meso" electrodes with a double layer electrode coating to create a pH-sensitive electrode. The sensing layer was iridium oxide (IrOx); it was modified with a H^+-ionophore-based H^+-selective membrane. The pH sensitive electrode was characterized *in vitro* and *in vivo*. *Main results.* The pH-sensitive electrode exhibited a pH sensitivity of -57.48 mV/pH during benchtop characterization and *in vivo* pH monitoring during CO_2 inhalation experiments predictably elicited immediate acidification. Concurrent pH changes and seizure activity were detected during pilocarpine-induced seizures. We were able to correlate an acidic spike of 0.024 pH with a significant electrical discharge we characterized as a seizure event. *Significance.* Previous studies had monitored pH and electrical activity only using intracortical penetrating electrodes. The modified multi-scale array is the first to simultaneously monitor pH changes and electrical activity

on the cortical surface from adjacent regions. The correlation of cortical pH changes with recorded seizure events validates the work from previous studies indicating that there are multiple biomarkers of epileptic activity. Additional electrodes are necessary to provide a greater understanding of localizing the origin of seizures. Combining ECoG and pH functionality within a single epidural electrode array for multi-species recordings will give us better insight into the timing and response between seizure onset, EEG spikes, and pH spikes.

4.1 Introduction

Significant advancements in electrode technology for neural monitoring from conventional EEG to micro-ECoG arrays to multi-functional microelectrode arrays are facilitating the diagnosis and treatment of neurological diseases previously thought to be intractable (Driscoll et al. 2021; Kwon et al. 2021; Raimondo et al. 2015; Vomero et al. 2020). Researchers have been exploring the use of various biomarkers to enhance the monitoring capabilities of existing electrodes or create additional capabilities that aid in neural diagnostics (Venkatraman et al. 2011).

Advancements in neural sensing and signal analysis have enabled better identification of seizures and treatment of epilepsy. While electrophysiological signals detected using intracortical electrode arrays remain the gold standard of seizure monitoring, other biomarkers such as miRNA detected in patients' blood samples or imaging biomarkers like GABA-A receptor density using positron emission tomography (PET) have not demonstrated a significant improvement in localizing the epileptogenic zone (Reddy et al. 2019; Kobylarek et al. 2019). Cerebrospinal fluid (CSF) has emerged as a promising source for potential biomarkers linked to epilepsy. The CSF's chemical

composition closely reflects the brain's biochemical makeup; it can indicate clinically relevant epileptic changes the brain (Hanin et al. 2020). Brain pH is thought to play a significant role in epilepsy, with pH regulation during seizures remaining poorly understood. Previous studies have shown that alkalosis of the brain enhances neuronal activity and could play a role in eliciting seizures (Chesler and Kaila 1992; Chesler 2003; Traub et al. 2020). In contrast, inhalation of carbon dioxide (CO_2) has been shown to decrease pH and act as a fast-acting anti-convulsant (Yang et al. 2014). The correlation between pH change and shifts in neuronal activity has been hypothesized to be related to a specific acid-sensing channel susceptible to extracellular pH change that regulated neuron excitability. Ziemann et al. (2008) found that acid-sensing ion channel 1a (ASIC1a) plays a vital role in reducing the frequency of seizures and seizure termination. These findings identified a molecular mechanism for seizure termination through extracellular acidosis that could provide an additional diagnosis strategy for drug-resistant epileptic patients.

Based on these findings, we aimed to modify a flexible micro-electrode array to enable pH sensing within the same array. This modified array provides multi-channel recording of electrophysiological activity and extracellular pH change *in vivo*. The platinum electrode array was described along with the fabrication process in (Yeh et al. 2020). The multi-species detection was demonstrated with two 1 mm diameter Pt electrodes from the multi-scale micro-ECoG array. One electrode was coated with the iridium oxide (IrOx) and H^+-ionophore-based polymer coating, while the other was left unmodified. Traditionally, glass electrodes are employed for pH, but they are often too cumbersome for biological applications due to the bulkiness and need for constant re-calibration. As micro and nanofabrication processes become more refined and ion-selective materials more abundant, exploring the integration has been of

continuous interest. We have selected materials and methods that enable pH sensing through modification of a microfabricated array rather than designing a independent sensor. This allows us to perform multi-species recordings with a single electronic interface and data acquisition setup, IrOx sensor and H^+-ionophore-based membrane. IrOx has been used in many neural recording and stimulation applications for its low impedance, high storage capacity, excellent biocompatibility, ease of deposition, and pH sensing properties (Meyer et al. 2001; Cork et al. 2017). The H^+-ionophore-based electrode coating is a polymeric ion-selective membrane that exhibits strong anti-fouling, high selectivity, sensitivity, and response time (Hao et al. 2016).

We report a novel and effective experimental design that demonstrates, for the first time, an *in vivo* potentiometric method for pH recording on the cortical surface of a live rat brain with simultaneous monitoring of electrophysiological signals during pilocarpine-induced seizure activity. The concurrent measurements highlight the relationship between electrical discharges commonly characterized as seizure activity and pH changes. This approach provides a minimally invasive method for simultaneously monitoring pH change on the brain's surface and can facilitate future research on other physiological processes associated with epileptic activity.

4.2 Materials and Methods

4.2.1 Reagents and Solutions

Iridium tetrachloride ($IrCL_4$), oxalic acid, potassium carbonate (K_2CO_3), hydrogen ionophore I, bis(2-ethylhexyl)sebacate, potassium tetrakis(4-chlorophenyl), poly(vinyl chloride), ascorbic acid (AA), dopamine (DA), 5-hydroxytryptamine (5-HT),

3,4-dihydroxyphenylacetic acid (DOPAC), tetrahydrofuran (THF), sodium hydroxide (NaOH), monopotassium phosphate (KH_2PO_4), sodium chloride (NaCl), potassium chloride (KCl), dihydrogen phosphate (K_2PO_4), magnesium dichloride ($MgCl_2$), sodium sulfate (Na_2SO_4, and calcium chloride ($CaCl_2$) were all purchased from Sigma Aldrich and used as supplied. A stock solution of NaOH (0.2 M) was prepared before use. To simulate the cerebrospinal fluid (CSF), an artificial CSF solution was created from KH_2PO_4 (0.2 M) with NaCl (126 mM), KCl (2.4 mM), $MgCl_2$ (0.85 mM), Na_2SO_4 (0.5 mM), and $CaCl_2$ (1.1 mM) was prepared. Other chemicals were of at least analytical grade reagents and used as received. All aqueous solutions were prepared with Milli-Q water (18.2 MΩ·cm).

4.2.2 Fabrication of pH sensor

Surface and penetrating platinum electrodes were modified using iridium oxide (IrOx) and the hydrogen-ionophore-based membrane using the same protocol. The surface electrode described above is part of the multi-scale array with a 1 mm diameter and platinum top metal layer. The penetrating electrode is a 0.5 mm diameter wire that was coated to a depth of 3 mm. IrOx was deposited onto the electrode configured as the working electrode area via electrochemical deposition following an established protocol (Meyer et al. 2001). 4 mM iridium tetrachloride ($IrCl_4$) was dissolved in an aqueous solution of 40 mM oxalic acid with 340 mM potassium carbonate (K_2CO_3) added slowly to create a final solution pH of $\sim$ 10.3. The solution was allowed to sit for 48 hours before electrodeposition to allow the establishment of an equilibrium Ir^{3+}/Ir^{4+} ratio, which is necessary to obtain adherent coatings. Using a Squidstat Plus potentiostat (Admiral Instruments), we performed 50 triangle wave deposition

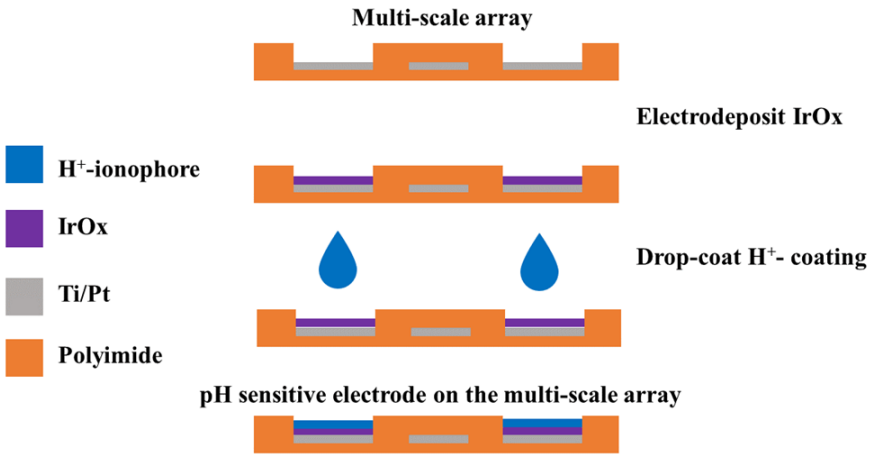

Figure 19. Fabrication overview of the pH sensitive electrode with the electrodeposition of IrOx on the Pt conductive layer of the multi-scale array followed by the drop-coating of the H^+-ionophore membrane.

cycles with potential varying between 0 and 0.55 V against a commercial Ag/AgCl reference electrode (3M KCl, BaSi) and a platinum coil counter electrode (BaSi) at 50 mV/s. Immediately following this, we pulsed square wave potentials for 3000 cycles with the same magnitude and a duration of 0.5 seconds each. Deposition took place in a 25°C water bath and each electrode was left to soak for 45 minutes post-deposition then stored in a dark room following removal from the deposition bath.

To ensure the pH-sensitive electrodes didn't experience ion interference from other analytes commonly found *in vivo*, a H^+-selective coating using hydrogen ionophore was prepared and applied atop the IrOx coating. The H^+-selective coating was prepared by dissolving hydrogen ionophore I (1.9 µl), bis(2-ethylhexyl) sebacate (100.0 mg), poly(vinyl chloride) (50.0 mg), KTpCIPB (1.0mg) in THF (1.5 ml). The solution was thoroughly mixed and drop cast onto the Pt wire and the microarray electrode until

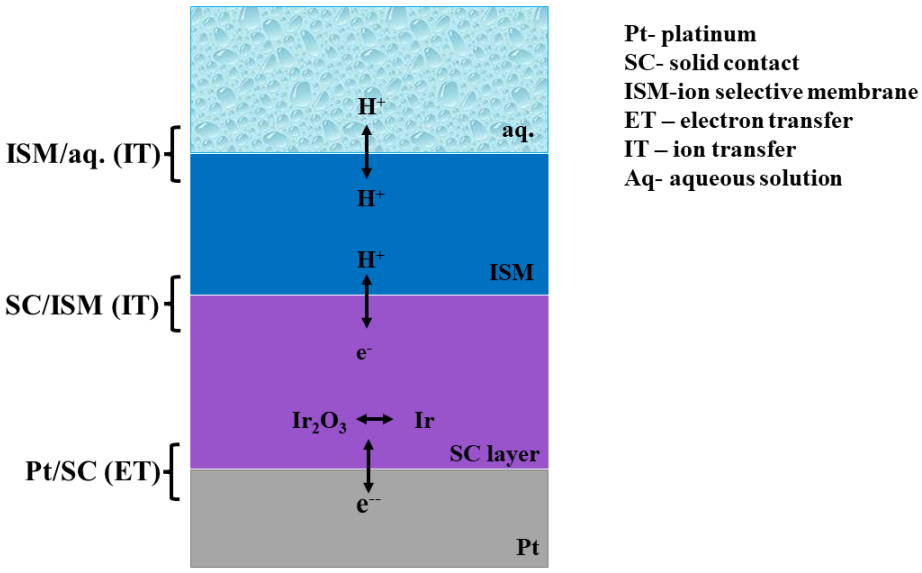

Figure 20. The pH response mechanism of hydrogen ionophore based ISEs. Pt-platinum electrode substrate; SC-solid contact; ISM-ion-selective membrane; ET-electron transfer; IT-ion transfer; aq-aqueous solution. Adapted from (Tang et al. 2022).

the solution evaporated. The coated electrodes were then conditioned in 1.0 x 10^{-3} M HCl for 12 hours before use.

4.2.3 pH sensing Mechanism

The sensing mechanism of the hydrogen ionophore based coating is described by classic ion-selective membrane (ISM) based solid contact (SC) ion-selective electrode (ISE) mechanisms. Using Pt as the electrode substrate and IrOx as the SC layer, the H^+ response mechanism is shown:

$$Ir_2O_3 + 6H^+ + 6e^- \rightleftharpoons 2Ir + 3H_2O \tag{4.1}$$

Equation 4.1 represents the redox equilibrium between two different solid phases of IrOx (i.e a higher and lower valence oxide) during the proton response indicated in Figure 20. Ir_2O_3 and Ir represent the oxide and pure metal state during the redox equilibrium. As the target H^+ ions come into contact with the ISM, the H^+ ions interact with the the hydrogen ionophores and pass through the membrane phase. Following this, the SC undergoes a redox reaction in which the target ions and protons are exchanged, converting the ionic signal into an electrical signal. The entire reaction involves the charge transfer balance of the Pt/SC, SC/ISM, and ISM/aq. interfaces. The total potential of the SC-ISEs is summarized as the Nernst equation related to the H^+ concentration in Equation 4.2:

$$E = E_{SC}^{Pt} \; + \; E_{ISM}^{SC} \; + \; E_{aq}^{ISM} \; = \; k \; + \; \frac{RT}{F} ln[H^+]_{aq} \tag{4.2}$$

where E_{SC}^{Pt}, E_{ISM}^{SC}, and E_{aq}^{ISM} are the interface potentials of Pt/SC, SC/ISM, and ISM/aq, respectively. R, T, and F represent the gas constant, temperature, and Faradaic constant, and $[H^+]_{aq}$ represents the concentration of H^+ in solution.

4.2.4 Sensor Characterization

4.2.4.1 Electrochemical Characterization

The Squidstat Plus was used for both EIS (electrochemical impedance spectroscopy) and CV (cyclic voltammetry). Characterization was performed in a phosphate buffered solution (PBS, 1M, pH 7.4) using a three-electrode cell consisting of the IrOx-coated electrode as the working electrode, Ag/AgCl reference electrode, and a platinum coil as the counter electrode was used for both measurements. EIS was performed by delivering a 10 mV RMS sinusoid to the working electrode from 0.5 Hz to 100 kHz.

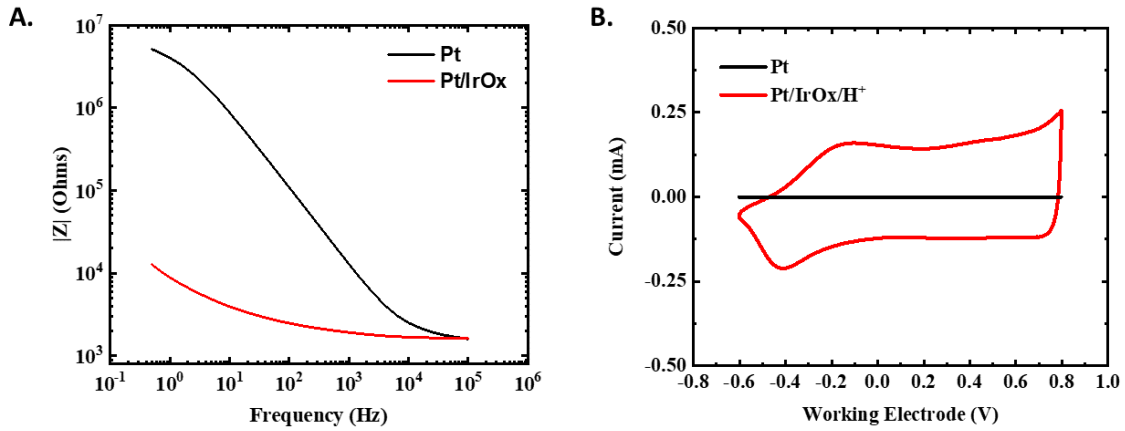

Figure 21. Electrochemical characterization of the pH-sensitive penetrating sensor: A. Complex magnitude bode plot of the bare Pt wire and the IrOx/H^+-selective coated Pt wire electrode. B. CV curves for the bare Pt and the IrOx/H^+-selective coated Pt wire.

CV was measured at a 50 mV/s rate between potential limits of -0.6 V and 0.8 V in the same three-electrode cell setup. Complex impedance magnitudes of the bare and IrOx/H^+-selective coated platinum wire are shown in Fig. 21A. At 1 kHz the bare Pt wire electrode has an impedance of 13 kΩ, while the coated Pt electrode has an impedance of 2 kΩ. The impedance differences between the bare and coated Pt wire electrodes within the 10 Hz - 10 kHz frequency range highlight the significance in the relevant neural recording frequency range.

The same electrochemical characterization was carried out for a bare surface electrode on the multi-scale array and an IrOx/H^+-selective coated 1 mm diameter electrode. Following the same electrodeposition protocol described previously, IrOx was electroplated onto the electrode and the H^+-selective coating was drop-coated on top of the IrOx-coated electrode. Complex magnitude impedance of the bare and coated surface electrodes are shown in Figure 22A. At 1 kHz the bare electrode exhibited an impedance of 4.4 kΩ while the coated electrode had an impedance of 2.2

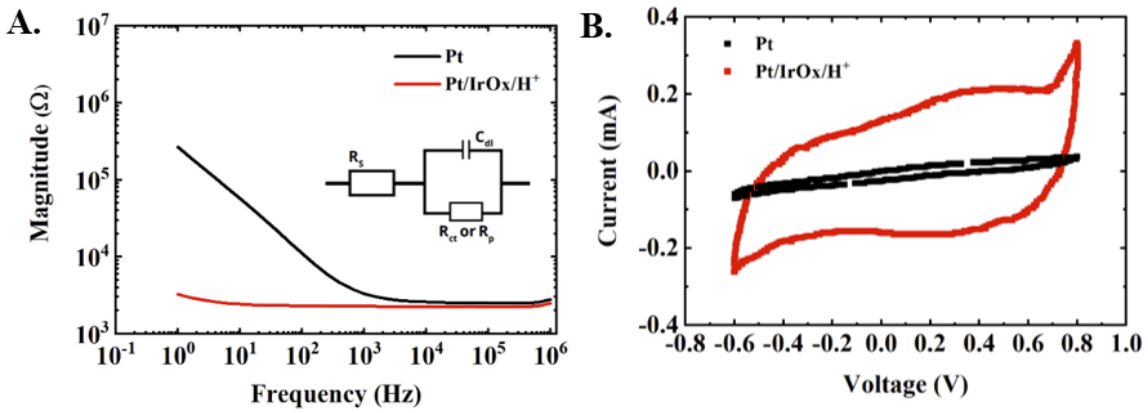

Figure 22. Electrochemical characterization of the pH-sensitive meso electrode: A. Complex magnitude bode plot of the bare Pt surface electrode and an $IrOx/H^+$-selective coated Pt surface electrode. B. CV curves for the bare Pt meso electrode and $IrOx/H^+$-selective coated Pt surface electrode.

kΩ. The $IrOx/H^+$-selective coating significantly reduced the impedance of the bare electrode as it did for the coated wire electrode. The CV plot for the surface electrode is shown in Figure 22B.

The equivalent circuit model of the electrode-electrolyte interface is shown in the inset of Figure 22A, where the R_s and R_{CT} are considered the solution resistance and charge transfer resistance, respectively. The constant phase element (CPE) was used in place of the double-layer capacitance (C_{dl}) to account for the =non-ideal capacitive response of the system. The CPE impedance is given by:

$$Z_{CPE} = \frac{1}{A(i\omega)^{\alpha}} \tag{4.3}$$

where A and α are frequency-independent parameter and $0 \leq \alpha \leq 1$, and ω is the angular frequency in rad/s. CPE would be considered an ideal capacitor if α=1 or purely resistive if α=0. R_s for both electrodes was 1.6±0.13 kΩ. As shown in Table 3, the larger α value indicates that the bare Pt electrode is smoother than the coated

Pt electrodes, and the decreased R_{CT} from 66.5 kΩ to 14.4±1.54 kΩ also indicates the increased surface roughness of the coated Pt electrode. At lower frequencies the impedance difference is significantly more pronounced as it's dominated by the capacitive coupling of the electrode double-layer, while at higher frequencies the impedance difference is negligible as the solution resistance dominates the impedance magnitude and both electrodes are in the same solution. CV curves of the bare Pt wire and coated Pt sensor in Fig. 21B show the increase in charge storage capacity (CSC) of the coated Pt sensor compared to the bare Pt electrode. The CSC of any implantable electrode is an important indicator and would justify investigating the performance of the sensor for neural stimulation in future work. The CSC is estimated by using the time integral of the cathodic current (area under the CV curve) given by equation 4.4 (Negi et al. 2010):

$$CSC = \frac{1}{vA} \int_{Ec}^{Ea} |i| \, dE \tag{4.4}$$

where E is the electrode potential, i is the measured current in amps, E_a and E_c are the anodic and cathodic potential limits in volts, A is the geometric surface area of the electrode, and v is the scan rate. The CV of the coated Pt wire-based sensor has a significantly larger internal area than the CV of the bare Pt wire electrode, indicating a higher CSC of the IrOx/H^+-selective electrode. The calculated CSC of the bare Pt electrode was found to be 245.32 µC/cm^2, while the CSC of the coated Pt wire sensor was found to be 9.84 mC/cm^2. The increase in CSC is due to the increase in the effective surface area from the electrodeposition of IrOx. This expected result shows that the coated Pt wire sensor would be great for neural stimulation which will be explored in future work.

Table 3. Fitting Results from EIS Model

Film	R^2	A(F)	α	R_{CT}
Pt	0.73	$3.08*10^{-6}$	0.92	66.5 kΩ
$Pt/H^+/IrOx$	0.86	$10.1*10^{-6}$	0.84	14.4 kΩ

4.2.4.2 Titration-based Sensitivity Characterization

Fine resolution characterization was performed using stepwise titration of the $IrOx/H^+$-selective surface (microarray) sensor was performed using potassium dihydrogen phosphate (K_2PO_4) and sodium hydroxide (NaOH). The temporal response to the step-like change in pH were examined and confirmed against a commercially pH electrode (Oakton Instruments). Figure 23 depicts the pH sensors sensitivity and potential response to pH stepwise pH changes. The stepwise response also indicated the temporal response of the pH electrode to elicited pH changes. The temporal response of the pH electrode was 2.1 seconds for a pH change of 0.2. The pH measurements were simultaneously monitored against a commercial pH electrode to ensure that pH recordings were accurate. These results verify the quick response of the $IrOx/H^+$-selective sensor to pH changes within the biologically relevant range.

The sensor sensitivity is determined by fitting the voltage v.s. pH curve. The Pt wire-based sensor fitted exhibited a slope of -69.54 mV/pH which is consistent with literature on the response for the H^+-selective coating and slightly super-Nernstian (Nernst potential is 59.1 mV/pH at 25 °C). The sensitivity of the $IrOx/H^+$ micro-array sensor was -57.48 mV/pH, very close to the Nernst potential.

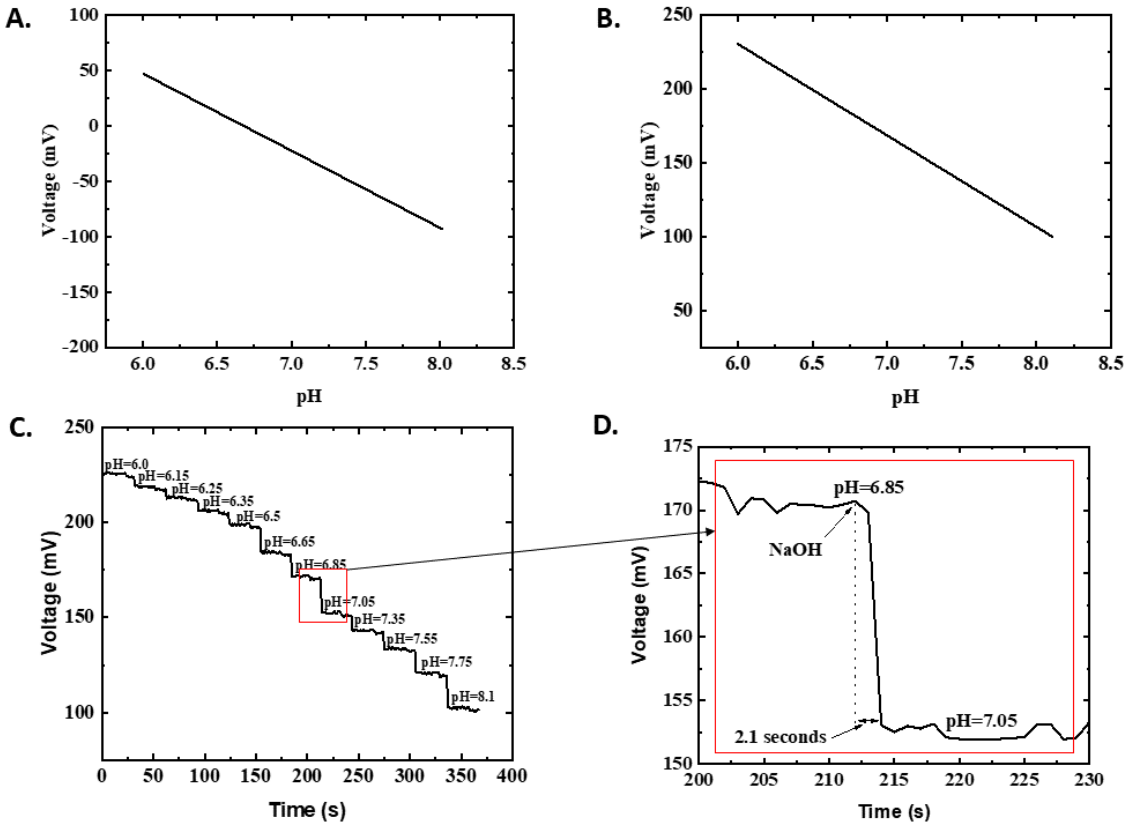

Figure 23. Potential response of the pH sensitive penetrating and meso electrode to a pH change using buffers. Sensitivity curves of the A. penetrating electrode and B. meso electrode. C. Potential response of the pH sensitive meso electrode to stepwise pH change. D. Time response of the indicated pH change from pH=6.85 to pH=7.05.

4.2.4.3 pH Sensor Specificity

The chemical and physiological complexity of the brain necessitates a highly selective pH sensor to achieve reproducible results. The specificity of the pH sensor was monitored against K^+ and Na^+, two of the most abundant ions in the brain. In addition, we tested some of the most common interferents typically present in the brain that decrease the specificity of neuro-sensors: ascorbic acid (AA), dopamine (DA), 3,4-Dihydroxyphenylacetic acid (DOPAC), and 5-hydroxytryptamine (5-HT), or serotonin (Hao et al. 2016; Jin, Li, and Jiang 2021). The coated microarray sensor was

submerged in artificial CSF with a pH of 7.4 and concentrations of 1 mM, 2mM, 4mM, and 10 mM of K^+ and Na^+ were sequentially added to determine the potential response to interfering ions. The open circuit potential (OCP) was monitored throughout each successive addition. Aside from a small transient response to the pipetting, the sensor showed no response to sodium or potassium ions. Separately, successive additions of 100 µM AA, 40 µM DOPAC, 10 µM DA, and 30 µM 5-HT were added to the coated sensor submerged in artificial CSF to examine the effect these chemicals to determine selectivity. The change in potential from the addition of these chemicals was compared against the potential change elicited from a 0.25 pH acidification from the addition of hydrochloric acid (HCl) as shown in Figure 24. From these measurements we can conclude the H^+-selective membrane is specific to H^+ ions and other biological molecules will not illicit a sensor response.

4.2.5 *In vivo* pH monitoring

All protocols for *in vivo* experiments were approved by the Institutional Animal Care and Use Committee of Arizona State University. To prepare for measurements, rats were anesthetized using an initial dose of 5% isoflurane and then placed in a stereotactic apparatus and maintained under anesthesia with a mixture of 2% isoflurane and continuous oxygen flowing at 2 liters per minute (lpm) delivered through a nose cone. Internal temperature was maintained with a heating pad and towels and monitored using a rectal probe. A single 5 mm x 10 mm window craniotomy was performed over the left hemisphere (coordinates with respect to bregma: 7 mm posterior, 3 mm anterior, 5.5 mm lateral, 0.5 mm medial) and the dura was carefully removed. The coated surface electrode on the multi-scale array was placed on the

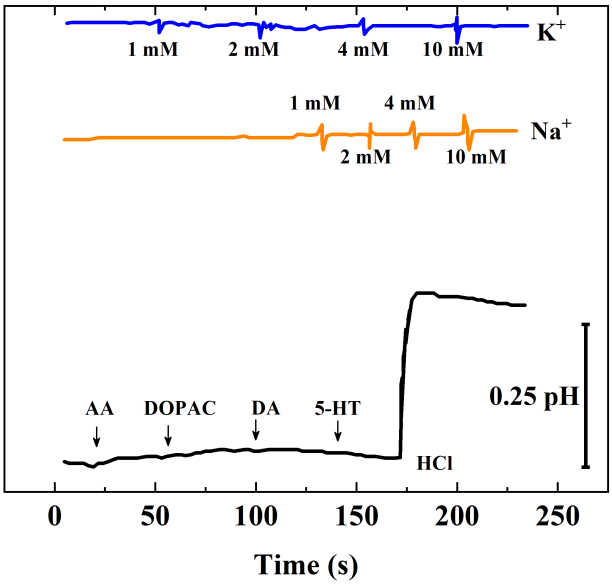

Figure 24. Potential response of the H^+-selective electrode on the multi-scale array towards increasing concentrations of K^+, Na^+ (blue trace, orange trace), ascorbic acid (AA), 3,4-dihydroxyphenylacetic acid (DOPAC), dopamine (DA), and 5-hydroxytryptamine (5-HT) (black trace) in artificial CSF solution (pH=7.4) as compared to a potential response from a 0.25 pH change

cortical surface followed by the insertion of the coated Pt wire sensor intracortically 4 mm away from the surface sensor as shown in Figure 25. OCP of both sensors was recorded to determine the change in pH throughout the experiment. The pH signals were amplified using a SR560 Low-noise amplifier (Stanford Research Systems, Sunnyvale, CA) and wired to a data acquisition system (DAQ) (National Instruments, Austin, TX).

4.2.5.1 CO_2-induced acid base disturbance

Four (two male, two female) Sprague-Dawley rats (250-350g) were used to determine whether pH changes could be detected *in vivo* using the custom fabricated pH surface

electrode. To demonstrating the ability to monitor pH changes *in vivo*, rats were subjected to CO_2 inhalation to evoke neural pH modulation (Magnotta et al. 2012; Esquivel et al. 2010). CO_2 inhalation has been noted to induce respiratory acidosis, elevating the arterial partial pressure of carbon dioxide (PCO_2) and decreasing the ratio of arterial bicarbonate to arterial PCO_2, thus lowering the blood pH. Figure 25 depicts the *in vivo* pH response when the animal is held under normal conditions (breathing O_2 with 2% isoflurane) and when pure CO_2 is inhaled for 30 second intervals (arrows). Breathing pure CO_2 rapidly decreased the pH of the coated wire-based sensor by 0.11 $\pm$ 0.02 pH and the microarray-based sensor by 0.03 $\pm$ 0.003. The results from the implanted penetrating electrode were consistent with previous studies and indicate the pH-sensitive coating used on the wire and surface electrode is capable of detecting pH changes from acid-base disturbances in the brain. Brain acidosis was induced by exposing the animal to three short intervals of 100% CO_2 inhalation for 30 seconds through the same nose cone oxygen was flowed through. Following CO_2 exposure, the animal was put back on oxygen and allowed to resume its normal respiratory rate and achieve baseline for at least 10 minutes before being exposed to the CO_2 inhalation again.

4.2.5.2 Simultaneous monitoring of pH and electrical activity during pilocarpine-induced seizure activity

Three (two male, one female) Sprague-Dawley rats (250-350 g) were used to correlate pH shifts with evoked seizure activity. Rats were anesthetized and maintained under anesthesia and craniotomy procedures and procedure outlined above. Two SR560 Low-noise amplifiers were connected to the data acquisition box and individually

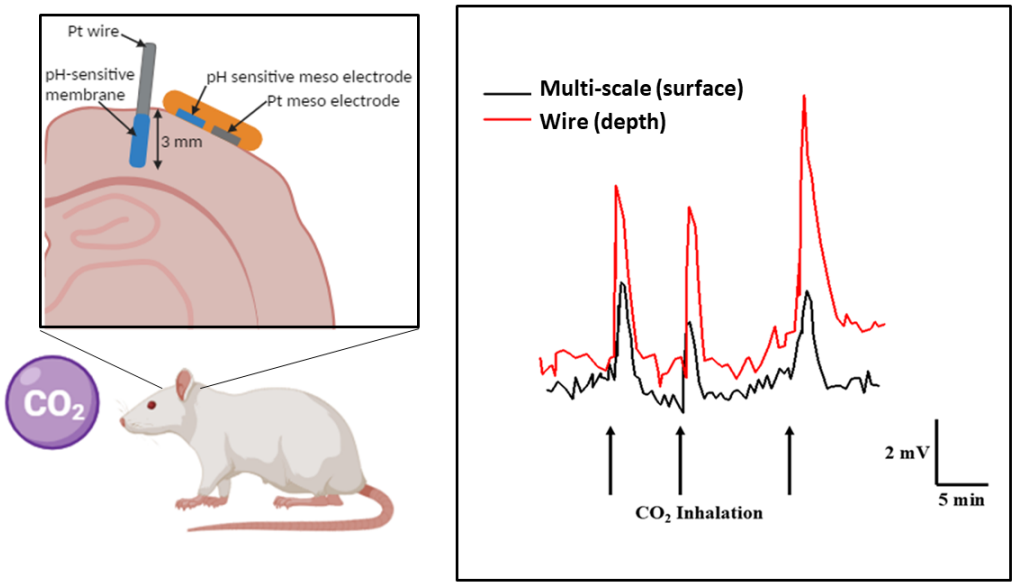

Figure 25. *In vivo* placement of the pH sensitive wire-based senosr and pH sensitive multi-scale flexible array sensor (left). Potential responses of the pH-sensitive wire and multi-scale sensors during brief CO_2 inhalation (right).

wired to each electrode. Five minutes of recording "typical" activity was completed to determine the baseline of neural and pH activity. 300 mg/kg of pilocarpine hydrochloride (Sigma Aldrich, St. Louis, MO, USA) was injected intraperitoneally to induced seizure activity. Neural signals were recorded with a 5 kHz sampling frequency and pH signals were recorded with a 50 Hz sampling frequency.

Pilocarpine-induced seizure activity was seen in each of the three rats during the simultaneous multi-species monitoring of neural activity and pH change using two 1 mm diameter electrodes on the multi-scale array, unmodified and IrOx/H^+-selective membrane coated. Figure 26 shows the raw pH signal (green) and neural activity (black) during the transition from pre-ictal (0-300 seconds) to interictal activity (300-650 seconds) and finally the post-ictal state (650-750 seconds). The transition from the preictal to interictal state was correlated to a decrease in pH (increase in

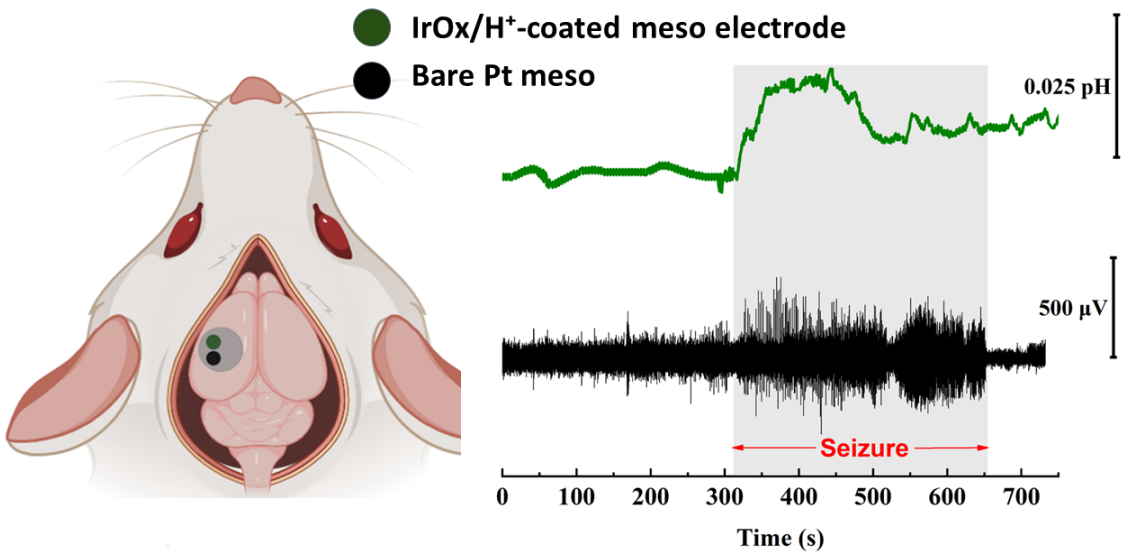

Figure 26. Placement of the multi-scale electrode with a pH sensitive meso electrode and bare Pt meso electrode (left). A sample recording of the simultaneous detection of pH response (green) and electrophysiological activity (black) during pilocarpine-induced seizure activity on the cortical surface (right).

voltage) of 0.025 ±0.005. The diminished pH value was maintained for 100 seconds and was gradually returned to near baseline as the seizure subsided. The appreciable change in pH during the transition from a resting to seizure state highlights the role ion dynamics plays in the generation, development, and termination of seizures. (Raimondo et al. 2015).

4.2.6 Post-operative Electrode Characterization

Sensor drift and degradation are consistent and significant sources of error for implantable sensors. We performed characterization of both the surface and penetrating electrodes before and after implant into the rodent model. This allowed us to determine whether the sensing surfaces were degraded by contact with or activity in the

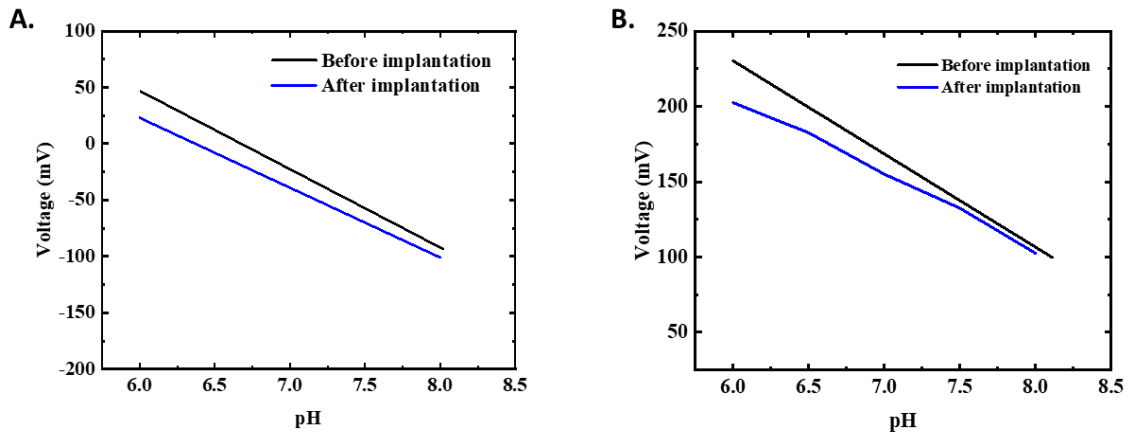

Figure 27. Both the (A.) penetrating and (B.) surface electrodes were characterized before and after *in vivo* placement of the pH sensitive wire and pH sensitive multi-scale electrode. The electrode open circuit potential was measured in pH 6, 7, 7.4, and 8 buffers.

neural tissue during sensing. The open circuit potential (OCP) was used to calibrate sensor pH against a standard Ag/AgCl reference electrode using pH buffers (pH: 6, 7, 7.4, and 8; Hanna Instruments) before and after *in vivo* implantation. Fig. 27A shows the sensitivity characterization of the wire-based sensor before (black) and after (blue) *in vivo* implantation using pH buffers 6, 7, 7.4, and 8. The OCP was measured three times for each buffer and the fitted curve exhibited a slope of -69.54 mV/pH pre-implantation and -66.67 mV/pH post-implantation, which is consistent with literature on the response for the H^+-selective coating and slightly super-Nernstian (Nernst potential is 59.1 mV/pH at 25 °C). The sensitivity of the H^+-sensitive surface electrode (Fig. 27B) was -57.48 mV/pH pre-implantation and -55.76 mV/pH post-implantation, which is consistent with the literature for this H^+-sensitive coating and a Nernstian response (i.e -59.1 mV/pH at 25 °C).

4.3 Discussion

In this study we successfully applied a multi-layer pH sensitive coating to an electrode on a flexible, multi-scale micro-ECoG array and monitored pH activity during CO_2 induced acid-base changes in anesthetized rats. Furthermore, we provided evidence for the first time of simultaneously monitoring neural electrical signals and pH activity on the cortical surface of pilocarpine-induced seizure activity in rats.

In previous studies, neuronal electrical activity has been coupled with *in vitro* extracellular pH shifts (Chesler 2003; Makani and Chesler 2010). IrOx on its own has been previously validated as an *in vivo* pH micro sensor (Marzouk et al. 1998; Kakooei, Ismail, and Ari-Wahjoedi 2013). ISMs based on hydrogen ionophores have also had recent success as *in vivo* pH sensors in the brain, however the combination of a multi-layer pH electrode fabricated with both IrOx and the H^+-ionophore-based ISM hasn't been previously reported in the literature. Monitoring pH in the brain had traditionally been realized by using penetrating electrodes or non-invasive imaging techniques like MRI. However, penetrating probes cause extensive tissue damage and imaging techniques are currently incapable of producing real-time results. In this study, we show the ability to perform real-time pH monitoring on surface of the brain using electrochemical detection while also demonstrating the ability to simultaneously monitor electrical activity on neighboring electrodes for multi-species detection.

pH plays an important role in modulating the excitability in neuronal circuits and thus plays a significant role in seizure termination. In general, alkalosis increases neuronal excitability and acidosis reduces neural excitability (Tolner et al. 2011). While previous studies highlighted this effect within the brain, our study aimed to demonstrate that similar reactions occurred on the surface of the brain. CO_2 inhalation

was performed to elicit immediate pH acidification and the penetrating wire electrode and surface electrode-based sensors both recorded decreases in pH. The pH decrease observed on the surface sensor was roughly a third of the pH change observed on the penetrating wire electrode. This difference of note because of the ion dynamics typically seen in the regulation of acid-base disturbances. We have shown for the first time simultaneous monitoring of pH changes from both locations. Mechanisms for pH regulation during CO_2 inhalation primarily occur due to the chemoreceptors governing pulmonary gas exchange (Siesjö 1972). However, the reason for the differences in pH change on the surface electrode and the pH change recorded on the penetrating electrode remains unclear.

The exploratory nature of the pH experiments on the cortical surface were heavily influenced by the presence of pH monitoring studies conducted at depth. These results do not attempt to differentiate between the recordings taken at different locations. Hypothesizing on the noticeable differences however leads us to multiple concerns. Concerns of electrode displacement on the surface of the brain are present, especially when the animal experiences rearing and shaking symptoms commonly seen in pilocarpine-induced seizures. Displacement of the electrode array would affect the pH recordings by impacting the physical contact of the electrode surface to the brains surface. Differences in pH response may also be a result of the differences in fluid concentrations inside the brain and on the surface. Future work can be directed toward this phenomena in order to determine the relationship between pH change at various depths and pH change on the cortical surface.

Concurrently recording electrophysiological activity and pH during seizure monitoring has been previously reported (Ziemann et al. 2008; Pavlov et al. 2013; Zhao et al. 2020). Treating patients with drug-resistant epilepsy has typically required

detection and removal of the epileptogenic region, which has come as a result of effective spatial mapping. These preliminary results provide evidence of an alternative monitoring technique on the surface of the brain that indicate the occurrence of abnormal neural activity. Lu et al. (2021) show that there are significant intracellular alkaline shifts in the brain in pilocarpine-model of mesial temporal lobe epilepsy. Our study is the first to verify that generalized regions on the surface of the brain experience acidic pH shifts as a result of seizure activity. These results could pave the way for less invasive monitoring of biochemical signals linked to neurological disorders. Identifying pH changes on the cortical surface using electrochemical techniques on modified micro-ECoG arrays opens the door to future studies that employ an array of pH-sensitive electrodes to eloquently map the pH change during brain events.

4.4 Conclusion

In summary, this study shows the creation of a novel flexible micro-ECoG array with the ability to simultaneously monitor pH and electrophysiological activity on the cortical surface of a live rat. Applying the IrOx and H^+-selective coating to an electrode on the multi-scale micro-ECoG array provides an example of a minimally invasive electrochemical pH monitoring system on the surface of the brain. Successfully monitoring pH change on the cortical surface using ionophore-based chemicals provides a clear avenue for monitoring other freely available organic ions commonly found *in vivo* such as K^+, Na^+, and Ca^{2+}. Utilizing a multi-species approach to monitoring pathological functions in the surface of brain during states of neural disorder, like during seizures, allows a broader investigation into identifying the mechanisms that lead to the termination or reduction of future events while minimizing the tissue

damage of the surrounding neural region. This study identifies the potential for future work to understand the roles that pH and other ions play during the physiological processes of neurological disorders without having to penetrate the brain.

Chapter 5

CONCLUSION AND PROPOSED FUTURE WORK

Numerous thin-film polymer electrode arrays have been introduced thus far to monitor neural signals and biological markers. This work, however, has gone beyond the conventional methods of designing, fabricating, and testing a novel multi-scale polyimide micro-ECoG array both *in vitro* and *in vivo*, and has produced some groundbreaking findings.

The unique, concentric microelectrode array design utilizing varying electrode geometries embedded in one another has been identified as the key factor in improving our understanding of how to enhance spatial resolution of neural activity and quantifying signals across multiple electrode arrays. The reliability and predictability of somatosensory evoked potentials made them the ideal choice for evaluating the spatial and temporal recording resolution. The SSEP's conducted on the multi-scale array verified the aggregate signal from the micro electrodes outperformed the larger meso and macro electrodes, which was then confirmed by a commercially available micro-ECoG array from Neuronexus. The results from the multi-scale array are conclusive in establishing that the micro electrodes had higher signal fidelity and greater spatial resolution than their encompassing meso and macro electrode counterparts.

The data gathered from our *in vitro* and *in vivo* experiments provide a solid foundation for understanding the spatial and temporal recording resolution of the novel embedded electrode design. Most thin-film micro-ECoG arrays to date have utilized uniform electrode sizes across a traditional grid layout. Hybrid arrays were seen as a possible way to obtain information that uniformly-sized arrays would not.

Without these experiments, we would have never known if the embedded electrode design of the multi-scale array was a viable option for monitoring neural signals. Our findings indicate that although useful information can be gathered from electrodes of varying sizes, an array of micro electrodes provides a greater basis for future work. This is due to the greater signal fidelity of higher frequency activity and improved spatial resolution of elicited activity.

We then used the pilocarpine-induced seizure model to reliably elicit epileptic activity and present similar electrical activity to those found in clinical seizures. The multi-scale array successfully detected electrographic seizures and confirmed with the Neuronexus array. This allowed us to confirm that multiple micro electrodes outperformed their larger electrode counterparts in recording HFO frequency range neurological signals.

Following the success of the multi-scale array in understanding trade-offs in electrode design for neural electrical signals, we went on to modify the multi-scale array to monitor pH change by electroplating an H^+-sensitive membrane on the Pt electrode surface. In our experiments, we investigated pH change on the surface of the brain and pH at depth using an electrode inserted into the cortex simultaneously. We used CO_2 inhalation to elicit an increase in pH *in vivo*. We observed CO_2 inhalation induced a noticeable pH change on the depth electrode while inducing a moderate pH change on the brain's surface. Additionally we observed pilocarpine-induced seizure activity invoked pH changes correlated with an increase in electrical activity. This correlation of pH change with electrical spiking on the surface of the brain has not been reported previously to our knowledge. This approach provides a minimally invasive technique for the multi-modal monitoring of neurological phenomena which has not previously explored.

In conclusion, we have explored the trade-offs in electrode array design for the recording of neurological signal across a range of clinically relevant frequencies. We have concluded that an array of micro-scale electrodes out-performs an equivalent area array of larger electrodes. Furthermore, we have demonstrated these electrode arrays can be modified to create multi-modal platforms that can be used to better understand neurological phenomena. We believe this work can better inform the design of multi-modal arrays. Future studies are needed to explore additional sensing modalities along with spatial distribution of the multi-modal sensors within the array. These studies would allow for better understanding of the spatial distribution of clinically relevant phenomena.

REFERENCES

Adelson, David, Peter McL. Black, Joseph R. Madsen, Uri Kramer, Mark A. Rockoff, James J. Riviello, Sandra L. Helmers, Mohamad Mikati, and Gregory L. Holmes. 1995. "Use of Subdural Grids and Strip Electrodes to Identify a Seizure Focus in Children" [in en]. *Pediatric Neurosurgery* 22 (4): 174–180. Accessed December 21, 2023. https://doi.org/10.1159/000120898.

Aregueta-Robles, Ulises A., Andrew J. Woolley, Laura A. Poole-Warren, Nigel H. Lovell, and Rylie A. Green. 2014. "Organic electrode coatings for next-generation neural interfaces." *Frontiers in Neuroengineering* 7 (May). Accessed December 21, 2023. https://doi.org/10.3389/fneng.2014.00015.

Behrens, E., J. Zentner, D. Van Roost, A. Hufnagel, C. E. Elger, and J. Schramm. 1994. "Subdural and depth electrodes in the presurgical evaluation of epilepsy" [in en]. *Acta Neurochirurgica* 128, nos. 1-4 (March): 84–87. Accessed December 21, 2023. https://doi.org/10.1007/BF01400656.

Beniczky, Sándor, Isa Conradsen, Oliver Henning, Martin Fabricius, and Peter Wolf. 2018. "Automated real-time detection of tonic-clonic seizures using a wearable EMG device" [in en]. *Neurology* 90, no. 5 (January). Accessed December 21, 2023. https://doi.org/10.1212/WNL.0000000000004893.

Blaschke, Benno M, Núria Tort-Colet, Anton Guimerà-Brunet, Julia Weinert, Lionel Rousseau, Axel Heimann, Simon Drieschner, et al. 2017. "Mapping brain activity with flexible graphene micro-transistors." *2D Materials* 4, no. 2 (February): 025040. Accessed November 15, 2023. https://doi.org/10.1088/2053-1583/aa5eff.

Bragin, A., C. L. Wilson, and J. Engel. 2000. "Chronic Epileptogenesis Requires Development of a Network of Pathologically Interconnected Neuron Clusters: A Hypothesis" [in en]. *Epilepsia* 41, no. s6 (June): S144–S152. Accessed July 13, 2023. https://doi.org/10.1111/j.1528-1157.2000.tb01573.x.

Bromfield, Edward B., José E. Cavazos, and Joseph I. Sirven. 2006. "Basic Mechanisms Underlying Seizures and Epilepsy" [in en]. In *An Introduction to Epilepsy [Internet].* American Epilepsy Society. Accessed October 24, 2023. https://www.ncbi.nlm.nih.gov/books/NBK2510/.

Campbell, P.K., K.E. Jones, R.J. Huber, K.W. Horch, and R.A. Normann. 1991. "A silicon-based, three-dimensional neural interface: manufacturing processes for an intracortical electrode array." *IEEE Transactions on Biomedical Engineering* 38,

no. 8 (August): 758–768. Accessed October 23, 2023. https://doi.org/10.1109/10.83588.

Castagnola, Elisa, Luca Maiolo, Emma Maggiolini, Antonio Minotti, Marco Marrani, Francesco Maita, Alessandro Pecora, et al. 2015. "PEDOT-CNT-Coated Low-Impedance, Ultra-Flexible, and Brain-Conformable Micro-ECoG Arrays." *IEEE Transactions on Neural Systems and Rehabilitation Engineering* 23, no. 3 (May): 342–350. Accessed December 13, 2023. https://doi.org/10.1109/TNSRE.2014.2342880.

Chari, Aswin, Rachel C Thornton, Martin M Tisdall, and Rodney C Scott. 2020. "Microelectrode recordings in human epilepsy: a case for clinical translation" [in en]. *Brain Communications* 2, no. 2 (July): fcaa082. Accessed July 12, 2023. https://doi.org/10.1093/braincomms/fcaa082.

Chen, Zhibin, Martin J. Brodie, Danny Liew, and Patrick Kwan. 2018. "Treatment Outcomes in Patients With Newly Diagnosed Epilepsy Treated With Established and New Antiepileptic Drugs: A 30-Year Longitudinal Cohort Study" [in en]. *JAMA Neurology* 75, no. 3 (March): 279. Accessed November 16, 2023. https://doi.org/10.1001/jamaneurol.2017.3949.

Chesler, M, and K Kaila. 1992. "Modulation of pH by neuronal activity." *Trends in neurosciences* 15 (10): 396–402.

Chesler, Mitchell. 2003. "Regulation and modulation of pH in the brain." *Physiological reviews* 83 (4): 1183–1221.

Cheung, Karen C. 2007. "Implantable microscale neural interfaces" [in en]. *Biomedical Microdevices* 9, no. 6 (October): 923–938. Accessed July 20, 2023. https://doi.org/10.1007/s10544-006-9045-z.

Clark, John W., Micheal R. Newman, Walter H. Olson, Robert A. Peura, Frank P. Primiano Jr., Melvin P. Siedband, John G. Webster, and Lawrence A. Wheeler. 2010. *Medical instrumentation: application and design.* 4th ed. Edited by John G. Webster. OCLC: ocn259902177. Hoboken, NJ: John Wiley & Sons.

Cork, Simon C, Amir Eftekhar, Khalid B Mirza, Claudio Zuliani, Konstantin Nikolic, James V Gardiner, Stephen R Bloom, and Christofer Toumazou. 2017. "Extracellular pH monitoring for use in closed-loop vagus nerve stimulation." *Journal of neural engineering* 15 (1): 016001.

Cornuéjols, Rémy, Amélie Albon, Suyash Joshi, James Alexander Taylor, Martin Baca, Sofia Drakopoulou, Tania Rinaldi Barkat, Christophe Bernard, and Shahab Rezaei-

Mazinani. 2023. “Design, Characterization, and In Vivo Application of Multi-Conductive Layer Organic Electrocorticography Probes” [in en]. *ACS Applied Materials & Interfaces* 15, no. 19 (May): 22854–22863. Accessed December 22, 2023. https://doi.org/10.1021/acsami.3c00553.

Curia, Giulia, Daniela Longo, Giuseppe Biagini, Roland S.G. Jones, and Massimo Avoli. 2008. *The pilocarpine model of temporal lobe epilepsy,* 2, July. https://doi.org/10.1016/j.jneumeth.2008.04.019.

Dai, Yuchuan, Yilin Song, Jingyu Xie, Shengwei Xu, Xinrong Li, Enhui He, Huabing Yin, and Xinxia Cai. 2021. “In Vivo Microelectrode Arrays for Detecting Multi-Region Epileptic Activities in the Hippocampus in the Latent Period of Rat Model of Temporal Lobe Epilepsy” [in en]. *Micromachines* 12, no. 6 (June): 659. Accessed December 21, 2023. https://doi.org/10.3390/mi12060659.

Dobrzynska, Jagoda A., and Martin A.M. Gijs. 2012. “Flexible polyimide-based force sensor” [in en]. *Sensors and Actuators A: Physical* 173, no. 1 (January): 127–135. Accessed July 11, 2023. https://doi.org/10.1016/j.sna.2011.11.006.

Driscoll, Nicolette, Richard E. Rosch, Brendan B. Murphy, Arian Ashourvan, Ramya Vishnubhotla, Olivia O. Dickens, A. T. Charlie Johnson, et al. 2021. “Multimodal in vivo recording using transparent graphene microelectrodes illuminates spatiotemporal seizure dynamics at the microscale.” *Communications Biology* 4, no. 1 (January 29, 2021): 136. Accessed October 16, 2023. https://doi.org/10.1038/s42003-021-01670-9.

Ein Shoka, Athar A., Mohamed M. Dessouky, Ayman El-Sayed, and Ezz El-Din Hemdan. 2023. “EEG seizure detection: concepts, techniques, challenges, and future trends” [in en]. *Multimedia Tools and Applications* 82, no. 27 (November): 42021–42051. Accessed December 21, 2023. https://doi.org/10.1007/s11042-023-15052-2.

Ellrich, Jens. 2020. “Cortical stimulation in pharmacoresistant focal epilepsies” [in en]. *Bioelectronic Medicine* 6, no. 1 (December): 19. Accessed December 22, 2023. https://doi.org/10.1186/s42234-020-00054-4.

Enatsu, Rei, Kazutaka Jin, Sherif Elwan, Yuichi Kubota, Zhe Piao, Timothy O’Connor, Karl Horning, Richard C Burgess, William Bingaman, and Dileep R Nair. 2012. “Correlations between ictal propagation and response to electrical cortical stimulation: a cortico-cortical evoked potential study.” *Epilepsy research* 101 (1-2): 76–87.

Engel, Jonathan, Jack Chen, and Chang Liu. 2003. "Development of polyimide flexible tactile sensor skin." *Journal of Micromechanics and Microengineering* 13, no. 3 (May): 359–366. Accessed July 11, 2023. https://doi.org/10.1088/0960-1317/13/3/302.

Englot, Dario J., and Edward F. Chang. 2014. "Rates and predictors of seizure freedom in resective epilepsy surgery: an update" [in en]. *Neurosurgical Review* 37, no. 3 (July): 389–405. Accessed November 16, 2023. https://doi.org/10.1007/s10143-014-0527-9.

Esquivel, G., Kr Schruers, Rj Maddock, A. Colasanti, and Ej Griez. 2010. "Review: Acids in the brain: a factor in panic?" *Journal of Psychopharmacology* 24, no. 5 (May): 639–647. Accessed October 16, 2023. https://doi.org/10.1177/0269881109104847.

Feigin, Valery L, Theo Vos, Fares Alahdab, Arianna Maever L Amit, Till Winfried Bärnighausen, Ettore Beghi, Mahya Beheshti, Prachi P Chavan, Michael H Criqui, Rupak Desai, et al. 2021. "Burden of neurological disorders across the US from 1990-2017: a global burden of disease study." *JAMA neurology* 78 (2): 165–176.

Geddes, Leslie A, and R Roeder. 2003. "Criteria for the selection of materials for implanted electrodes." *Annals of biomedical engineering* 31:879–890.

González, Oscar C., Giri P. Krishnan, Igor Timofeev, and Maxim Bazhenov. 2019. "Ionic and synaptic mechanisms of seizure generation and epileptogenesis" [in en]. *Neurobiology of Disease* 130 (October): 104485. Accessed December 21, 2023. https://doi.org/10.1016/j.nbd.2019.104485.

Green, Rylie, and Mohammad Reza Abidian. 2015. "Conducting Polymers for Neural Prosthetic and Neural Interface Applications" [in en]. *Advanced Materials* 27, no. 46 (December): 7620–7637. Accessed December 21, 2023. https://doi.org/10.1002/adma.201501810.

Gulino, Maurizio, Donghoon Kim, Salvador Pané, Sofia Duque Santos, and Ana Paula Pêgo. 2019. "Tissue Response to Neural Implants: The Use of Model Systems Toward New Design Solutions of Implantable Microelectrodes." *Frontiers in Neuroscience* 13 (July): 689. Accessed July 13, 2023. https://doi.org/10.3389/fnins.2019.00689.

Gupta, Kanupriya, Pulkit Grover, and Taylor J. Abel. 2020. "Current Conceptual Understanding of the Epileptogenic Network From Stereoelectroencephalography-Based Connectivity Inferences." *Frontiers in Neurology* 11 (November): 569699. Accessed December 21, 2023. https://doi.org/10.3389/fneur.2020.569699.

Haas, L F. 2003. "Hans Berger (1873-1941), Richard Caton (1842-1926), and electroencephalography." *Journal of Neurology, Neurosurgery & Psychiatry* 74, no. 1 (January): 9–9. Accessed December 21, 2023. https://doi.org/10.1136/jnnp.74.1.9.

Hanin, Aurélie, Virginie Lambrecq, Jérôme Alexandre Denis, Françoise Imbert-Bismut, Benoît Rucheton, Foudil Lamari, Dominique Bonnefont-Rousselot, Sophie Demeret, and Vincent Navarro. 2020. "Cerebrospinal fluid and blood biomarkers of status epilepticus" [in en]. *Epilepsia* 61, no. 1 (January): 6–18. Accessed December 26, 2023. https://doi.org/10.1111/epi.16405.

Hao, Jie, Tongfang Xiao, Fei Wu, Ping Yu, and Lanqun Mao. 2016. "High antifouling property of ion-selective membrane: toward in vivo monitoring of pH change in live brain of rats with membrane-coated carbon fiber electrodes." *Analytical chemistry* 88 (22): 11238–11243.

Hasegawa, Daisuke. 2016. "Diagnostic techniques to detect the epileptogenic zone: Pathophysiological and presurgical analysis of epilepsy in dogs and cats" [in en]. *The Veterinary Journal* 215 (September): 64–75. Accessed November 16, 2023. https://doi.org/10.1016/j.tvjl.2016.03.005.

He, Guangwei, Xufeng Dong, and Min Qi. 2020. "From the perspective of material science: a review of flexible electrodes for brain-computer interface." *Materials Research Express* 7, no. 10 (October): 102001. Accessed October 24, 2023. https://doi.org/10.1088/2053-1591/abb857.

Ho, Kevin, Nicholas Lawn, Michael Bynevelt, Judy Lee, and John Dunne. 2013. "Neuroimaging of first-ever seizure: Contribution of MRI if CT is normal" [in en]. *Neurology Clinical Practice* 3, no. 5 (October): 398–403. Accessed December 21, 2023. https://doi.org/10.1212/CPJ.0b013e3182a78f25.

Hosp, Jonas A., Katiuska Molina-Luna, Benjamin Hertler, Clement Osei Atiemo, Alfred Stett, and Andreas R. Luft. 2008. "Thin-film epidural microelectrode arrays for somatosensory and motor cortex mapping in rat" [in en]. *Journal of Neuroscience Methods* 172, no. 2 (July): 255–262. Accessed March 27, 2023. https://doi.org/10.1016/j.jneumeth.2008.05.010.

Jacobs, J., R. Staba, E. Asano, H. Otsubo, J.Y. Wu, M. Zijlmans, I. Mohamed, et al. 2012. "High-frequency oscillations (HFOs) in clinical epilepsy" [in en]. *Progress in Neurobiology* 98, no. 3 (September): 302–315. Accessed December 21, 2023. https://doi.org/10.1016/j.pneurobio.2012.03.001.

Jacobs, Julia, and Maeike Zijlmans. 2020. "HFO to Measure Seizure Propensity and Improve Prognostication in Patients With Epilepsy" [in en]. *Epilepsy Currents*

20, no. 6 (November): 338–347. Accessed December 13, 2023. https://doi.org/10.1177/1535759720957308.

Jehi, Lara. 2018. "The Epileptogenic Zone: Concept and Definition" [in en]. *Epilepsy Currents* 18, no. 1 (February): 12–16. Accessed November 16, 2023. https://doi.org/10.5698/1535-7597.18.1.12.

Jin, Ying, Xin Li, and Ying Jiang. 2021. "Selectively probing neurochemicals in living animals with electrochemical systems." *ChemNanoMat* 7 (5): 489–501.

Jiruska, Premysl, Catalina Alvarado-Rojas, Catherine A. Schevon, Richard Staba, William Stacey, Fabrice Wendling, and Massimo Avoli. 2017. "Update on the mechanisms and roles of high-frequency oscillations in seizures and epileptic disorders" [in en]. *Epilepsia* 58, no. 8 (August): 1330–1339. Accessed December 21, 2023. https://doi.org/10.1111/epi.13830.

Jiruska, Premysl, and Anatol Bragin. 2011. "High-frequency activity in experimental and clinical epileptic foci" [in en]. *Epilepsy Research* 97, no. 3 (December): 300–307. Accessed October 25, 2023. https://doi.org/10.1016/j.eplepsyres.2011.09.023.

Kakooei, Saeid, Mokhtar Che Ismail, and Bambang Ari-Wahjoedi. 2013. "An overview of pH sensors based on iridium oxide: fabrication and application." *Int. J. Mater. Sci. Innov* 1 (1): 62–72.

Kalilani, Linda, Xuezheng Sun, Barbara Pelgrims, Matthias Noack-Rink, and Vicente Villanueva. 2018. "The epidemiology of drug-resistant epilepsy: A systematic review and meta-analysis" [in en]. *Epilepsia* 59, no. 12 (December): 2179–2193. Accessed October 25, 2023. https://doi.org/10.1111/epi.14596.

Khodagholy, Dion, Thomas Doublet, Pascale Quilichini, Moshe Gurfinkel, Pierre Leleux, Antoine Ghestem, Esma Ismailova, et al. 2013. "In vivo recordings of brain activity using organic transistors" [in en]. *Nature Communications* 4, no. 1 (March): 1575. Accessed December 21, 2023. https://doi.org/10.1038/ncomms2573.

Khodagholy, Dion, Jennifer N Gelinas, Thomas Thesen, Werner Doyle, Orrin Devinsky, George G Malliaras, and György Buzsáki. 2015. "NeuroGrid: recording action potentials from the surface of the brain" [in en]. *Nature Neuroscience* 18, no. 2 (February): 310–315. Accessed July 11, 2023. https://doi.org/10.1038/nn.3905.

Kim, Dong-Hwan, James A. Wiler, David J. Anderson, Daryl R. Kipke, and David C. Martin. 2010. "Conducting polymers on hydrogel-coated neural electrode provide sensitive neural recordings in auditory cortex" [in en]. *Acta Biomaterialia* 6, no. 1

(January): 57–62. Accessed December 21, 2023. https://doi.org/10.1016/j.actbio.2009.07.034.

Kim, Geon, Kanghyun Kim, Eunji Lee, Taechang An, WooSeok Choi, Geunbae Lim, and Jung Shin. 2018. "Recent Progress on Microelectrodes in Neural Interfaces" [in en]. *Materials* 11, no. 10 (October): 1995. Accessed August 7, 2023. https://doi.org/10.3390/ma11101995.

Kinoshita, Masako, Akio Ikeda, Masao Matsuhashi, Riki Matsumoto, Takefumi Hitomi, Tahamina Begum, Keiko Usui, Motohiro Takayama, Nobuhiro Mikuni, Susumu Miyamoto, et al. 2005. "Electric cortical stimulation suppresses epileptic and background activities in neocortical epilepsy and mesial temporal lobe epilepsy." *Clinical neurophysiology* 116 (6): 1291–1299.

Kipke, D.R., R.J. Vetter, J.C. Williams, and J.F. Hetke. 2003. "Silicon-substrate intracortical microelectrode arrays for long-term recording of neuronal spike activity in cerebral cortex." *IEEE Transactions on Neural Systems and Rehabilitation Engineering* 11, no. 2 (June): 151–155. Accessed October 23, 2023. https://doi.org/10.1109/TNSRE.2003.814443.

Kobylarek, Dominik, Piotr Iwanowski, Zuzanna Lewandowska, Nattakarn Limphaibool, Sara Szafranek, Anita Labrzycka, and Wojciech Kozubski. 2019. "Advances in the Potential Biomarkers of Epilepsy." *Frontiers in Neurology* 10 (July): 685. Accessed December 26, 2023. https://doi.org/10.3389/fneur.2019.00685.

Kovac, Stjepana, Philippe Kahane, and Beate Diehl. 2016. "Seizures induced by direct electrical cortical stimulation – Mechanisms and clinical considerations." *Clinical Neurophysiology* 127 (1): 31–39. https://doi.org/https://doi.org/10.1016/j.clinph.2014.12.009.

Kozai, Takashi D Yoshida, Nicholas B Langhals, Paras R Patel, Xiaopei Deng, Huanan Zhang, Karen L Smith, Joerg Lahann, Nicholas A Kotov, and Daryl R Kipke. 2012. "Ultrasmall implantable composite microelectrodes with bioactive surfaces for chronic neural interfaces." *Nature materials* 11 (12): 1065–1073.

Kozai, Takashi D. Y., Andrea S. Jaquins-Gerstl, Alberto L. Vazquez, Adrian C. Michael, and X. Tracy Cui. 2015. "Brain Tissue Responses to Neural Implants Impact Signal Sensitivity and Intervention Strategies" [in en]. *ACS Chemical Neuroscience* 6, no. 1 (January): 48–67. Accessed December 21, 2023. https://doi.org/10.1021/cn500256e.

Kwon, Yong Won, Yoon Sun Jun, Young-Geun Park, Jiuk Jang, and Jang-Ung Park. 2021. "Recent advances in electronic devices for monitoring and modulation of

brain." *Nano Research* 14, no. 9 (September): 3070–3095. Accessed October 16, 2023. https://doi.org/10.1007/s12274-021-3476-y.

Landazuri, Patrick, Jerry Shih, Eric Leuthardt, Sharona Ben-Haim, Joseph Neimat, Zulma Tovar-Spinoza, Veronica Chiang, et al. 2020. "A prospective multicenter study of laser ablation for drug resistant epilepsy – One year outcomes" [in en]. *Epilepsy Research* 167 (November): 106473. Accessed November 16, 2023. https://doi.org/10.1016/j.eplepsyres.2020.106473.

Lee, Jung Min, Young-Woo Pyo, Yeon Jun Kim, Jin Hee Hong, Yonghyeon Jo, Wonshik Choi, Dingchang Lin, and Hong-Gyu Park. 2023. "The ultra-thin, minimally invasive surface electrode array NeuroWeb for probing neural activity" [in en]. *Nature Communications* 14, no. 1 (November): 7088. Accessed November 16, 2023. https://doi.org/10.1038/s41467-023-42860-9.

Lenihan, T., L. Schaper, Y. Shi, G. Morcan, and J. Parkerson. 1996. "Embedded thin film resistors, capacitors and inductors in flexible polyimide films." In *1996 Proceedings 46th Electronic Components and Technology Conference,* 119–124. Orlando, FL, USA: IEEE. Accessed July 11, 2023. https://doi.org/10.1109/ECTC.1996.517382.

Li, Xinrong, Yilin Song, Guihua Xiao, Enhui He, Jingyu Xie, Yuchuan Dai, Yu Xing, et al. 2021. "PDMS–Parylene Hybrid, Flexible Micro-ECoG Electrode Array for Spatiotemporal Mapping of Epileptic Electrophysiological Activity from Multicortical Brain Regions" [in en]. *ACS Applied Bio Materials* 4, no. 11 (November): 8013–8022. Accessed August 31, 2023. https://doi.org/10.1021/acsabm.1c00923.

Lopez, Carolina Mora, Alexandru Andrei, Srinjoy Mitra, Marleen Welkenhuysen, Wolfgang Eberle, Carmen Bartic, Robert Puers, Refet Firat Yazicioglu, and Georges G. E. Gielen. 2014. "An Implantable 455-Active-Electrode 52-Channel CMOS Neural Probe." *IEEE Journal of Solid-State Circuits* 49, no. 1 (January): 248–261. Accessed October 12, 2023. https://doi.org/10.1109/JSSC.2013.2284347.

Lu, Dongshuang, Yang Ji, Padmavathi Sundaram, Roger D. Traub, Yuguang Guan, Jian Zhou, Tianfu Li, Phillip Zhe Sun, Guoming Luan, and Yoshio Okada. 2021. "Alkaline brain pH shift in rodent lithium-pilocarpine model of epilepsy with chronic seizures" [in en]. *Brain Research* 1758 (May): 147345. Accessed December 21, 2023. https://doi.org/10.1016/j.brainres.2021.147345.

Luan, Lan, Xiaoling Wei, Zhengtuo Zhao, Jennifer J. Siegel, Ojas Potnis, Catherine A Tuppen, Shengqing Lin, et al. 2017. "Ultraflexible nanoelectronic probes form reliable, glial scar–free neural integration" [in en]. *Science Advances* 3, no. 2

(February): e1601966. Accessed December 21, 2023. https://doi.org/10.1126/sciadv.1601966.

Lüders, Hans, Ronald P Lesser, Dudley S Dinner, Harold H Morris, Elaine Wyllie, and Jaime Godoy. 1988. "Localization of cortical function: new information from extraoperative monitoring of patients with epilepsy." *Epilepsia* 29:S56–S65.

Magnotta, Vincent A., Hye-Young Heo, Brian J. Dlouhy, Nader S. Dahdaleh, Robin L. Follmer, Daniel R. Thedens, Michael J. Welsh, and John A. Wemmie. 2012. "Detecting activity-evoked pH changes in human brain." *Proceedings of the National Academy of Sciences* 109, no. 21 (May 22, 2012): 8270–8273. Accessed October 16, 2023. https://doi.org/10.1073/pnas.1205902109.

Makani, Sachin, and Mitchell Chesler. 2010. "Rapid rise of extracellular pH evoked by neural activity is generated by the plasma membrane calcium ATPase." *Journal of neurophysiology* 103 (2): 667–676.

Malmgren, Kristina, and Anna Edelvik. 2017. "Long-term outcomes of surgical treatment for epilepsy in adults with regard to seizures, antiepileptic drug treatment and employment" [in en]. *Seizure* 44 (January): 217–224. Accessed November 16, 2023. https://doi.org/10.1016/j.seizure.2016.10.015.

Marzouk, Sayed A. M., Stefan Ufer, Richard P. Buck, Timothy A. Johnson, Larry A. Dunlap, and Wayne E. Cascio. 1998. "Electrodeposited Iridium Oxide pH Electrode for Measurement of Extracellular Myocardial Acidosis during Acute Ischemia." *Analytical Chemistry* 70, no. 23 (December 1, 1998): 5054–5061. Accessed March 27, 2023. https://doi.org/10.1021/ac980608e.

Matteucci, Paul B., Alejandro Barriga-Rivera, Calvin D. Eiber, Nigel H. Lovell, John W. Morley, and Gregg J. Suaning. 2016. "The Effect of Electric Cross-Talk in Retinal Neurostimulation." *Investigative Opthalmology & Visual Science* 57, no. 3 (March 8, 2016): 1031. Accessed October 12, 2023. https://doi.org/10.1167/iovs.15-18400.

Meyer, R.D., S.F. Cogan, T.H. Nguyen, and R.D. Rauh. 2001. "Electrodeposited iridium oxide for neural stimulation and recording electrodes." *IEEE Transactions on Neural Systems and Rehabilitation Engineering* 9, no. 1 (March): 2–11. Accessed March 27, 2023. https://doi.org/10.1109/7333.918271.

Moncion, Carolina, Lakshmini Balachandar, Satheesh Bojja Venkatakrishnan, John L. Volakis, and Jorge Riera Diaz. 2022. "Multichannel Wireless Neurosensing System for battery-free monitoring of neuronal activity" [in en]. *Biosensors and*

Bioelectronics 213 (October): 114455. Accessed May 1, 2023. https://doi.org/10.1016/j.bios.2022.114455.

Morrell, Martha J. 2011. "Responsive cortical stimulation for the treatment of medically intractable partial epilepsy" [in en]. *Neurology* 77, no. 13 (September): 1295–1304. Accessed December 13, 2023. https://doi.org/10.1212/WNL.0b013e3182302056.

Mulcahey, Patrick J., Yuzhang Chen, Nicolette Driscoll, Brendan B. Murphy, Olivia O. Dickens, A. T. Charlie Johnson, Flavia Vitale, and Hajime Takano. 2022. "Multimodal, Multiscale Insights into Hippocampal Seizures Enabled by Transparent, Graphene-Based Microelectrode Arrays" [in en]. *eneuro* 9, no. 3 (May): ENEURO.0386–21.2022. Accessed December 21, 2023. https://doi.org/10.1523/ENEURO.0386-21.2022.

Negi, S, R Bhandari, L Rieth, and F Solzbacher. 2010. "*In vitro* comparison of sputtered iridium oxide and platinum-coated neural implantable microelectrode arrays." *Biomedical Materials* 5, no. 1 (February): 015007. Accessed September 1, 2023. https://doi.org/10.1088/1748-6041/5/1/015007.

Obien, Marie Engelene J., Kosmas Deligkaris, Torsten Bullmann, Douglas J. Bakkum, and Urs Frey. 2015. "Revealing neuronal function through microelectrode array recordings." *Frontiers in Neuroscience* 8 (January). Accessed December 21, 2023. https://doi.org/10.3389/fnins.2014.00423.

Ortiz-Catalan, Max, Rickard Brånemark, Bo Håkansson, and Jean Delbeke. 2012. "On the viability of implantable electrodes for the natural control of artificial limbs: review and discussion." *Biomedical engineering online* 11 (1): 1–24.

Park, Chae Jung, and Seung Bong Hong. 2019. "High Frequency Oscillations in Epilepsy: Detection Methods and Considerations in Clinical Application" [in en]. *Journal of Epilepsy Research* 9, no. 1 (January): 1–13. Accessed November 16, 2023. https://doi.org/10.14581/jer.19001.

Park, Yun S., G. Rees Cosgrove, Joseph R. Madsen, Emad N. Eskandar, Leigh R. Hochberg, Sydney S. Cash, and Wilson Truccolo. 2020. "Early Detection of Human Epileptic Seizures Based on Intracortical Microelectrode Array Signals." *IEEE Transactions on Biomedical Engineering* 67, no. 3 (March): 817–831. Accessed December 21, 2023. https://doi.org/10.1109/TBME.2019.2921448.

Pavlov, Ivan, Kai Kaila, Dimitri M. Kullmann, and Richard Miles. 2013. "Cortical inhibition, pH and cell excitability in epilepsy: what are optimal targets for antiepileptic interventions?" [In en]. *The Journal of Physiology* 591, no. 4 (February): 765–774. Accessed December 21, 2023. https://doi.org/10.1113/jphysiol.2012.237958.

Polikov, Vadim S., Patrick A. Tresco, and William M. Reichert. 2005. "Response of brain tissue to chronically implanted neural electrodes" [in en]. *Journal of Neuroscience Methods* 148, no. 1 (October): 1–18. Accessed December 21, 2023. https://doi.org/10.1016/j.jneumeth.2005.08.015.

Porto Cruz, Maria Francisca, Maria Vomero, Elena Zucchini, Emanuela Delfino, Maria Asplund, Thomas Stieglit, and Luciano Fadiga. 2019. "Can Crosstalk Compromise the Recording of High-Frequency Neural Signals?" In *2019 9th International IEEE/EMBS Conference on Neural Engineering (NER),* 924–927. 2019 9th International IEEE/EMBS Conference on Neural Engineering (NER). San Francisco, CA, USA: IEEE, March. Accessed October 12, 2023. https://doi.org/10.1109/NER.2019.8717009.

Prasad, Abhishek, and Justin C Sanchez. 2012. "Quantifying long-term microelectrode array functionality using chronic *in vivo* impedance testing." *Journal of Neural Engineering* 9, no. 2 (April): 026028. Accessed October 23, 2023. https://doi.org/10.1088/1741-2560/9/2/026028.

Raimondo, Joseph V., Richard J. Burman, Arieh A. Katz, and Colin J. Akerman. 2015. "Ion dynamics during seizures." *Frontiers in Cellular Neuroscience* 9 (October 21, 2015). Accessed March 27, 2023. https://doi.org/10.3389/fncel.2015.00419.

Ramgopal, Sriram, Sigride Thome-Souza, Michele Jackson, Navah Ester Kadish, Iván Sánchez Fernández, Jacquelyn Klehm, William Bosl, Claus Reinsberger, Steven Schachter, and Tobias Loddenkemper. 2014. "Seizure detection, seizure prediction, and closed-loop warning systems in epilepsy" [in en]. *Epilepsy & Behavior* 37 (August): 291–307. Accessed December 21, 2023. https://doi.org/10.1016/j.yebeh.2014.06.023.

Reddy, Sandesh, Iyan Younus, Vidya Sridhar, and Doodipala Reddy. 2019. "Neuroimaging Biomarkers of Experimental Epileptogenesis and Refractory Epilepsy" [in en]. *International Journal of Molecular Sciences* 20, no. 1 (January): 220. Accessed December 26, 2023. https://doi.org/10.3390/ijms20010220.

Rho, Jong M. 2009. "Arresting a Seizure by Dropping a Little Acid" [in en]. *Epilepsy Currents* 9, no. 2 (March): 55–56. Accessed April 18, 2023. https://doi.org/10.1111/j.1535-7511.2008.01291.x.

Romanelli, Pantaleo, Marco Piangerelli, David Ratel, Christophe Gaude, Thomas Costecalde, Cosimo Puttilli, Mauro Picciafuoco, Alim Benabid, and Napoleon Torres. 2019. "A novel neural prosthesis providing long-term electrocorticography recording and cortical stimulation for epilepsy and brain-computer interface."

Journal of Neurosurgery 130, no. 4 (April): 1166–1179. Accessed July 13, 2023. https://doi.org/10.3171/2017.10.JNS17400.

Roy, Trishit, and Alak Pandit. 2011. "Neuroimaging in epilepsy" [in en]. *Annals of Indian Academy of Neurology* 14 (2): 78. Accessed December 21, 2023. https://doi.org/10.4103/0972-2327.82787.

Rubehn, Birthe, Robert Oostenveld, Pascal Fries, and Thomas Stieglitz. 2009. "A MEMS-based flexible multichannel ECoG-electrode array." *Journal of Neural Engineering* 6, no. 3 (June 1, 2009): 036003. Accessed October 12, 2023. https://doi.org/10.1088/1741-2560/6/3/036003.

Ryvlin, Philippe, Sylvain Rheims, Lawrence J Hirsch, Arseny Sokolov, and Lara Jehi. 2021. "Neuromodulation in epilepsy: state-of-the-art approved therapies" [in en]. *The Lancet Neurology* 20, no. 12 (December): 1038–1047. Accessed November 16, 2023. https://doi.org/10.1016/S1474-4422(21)00300-8.

Scharfman, Helen E. 2007. "The neurobiology of epilepsy" [in en]. *Current Neurology and Neuroscience Reports* 7, no. 4 (July): 348–354. Accessed October 24, 2023. https://doi.org/10.1007/s11910-007-0053-z.

Schönberger, Jan, Charlotte Huber, Daniel Lachner-Piza, Kerstin Alexandra Klotz, Matthias Dümpelmann, Andreas Schulze-Bonhage, and Julia Jacobs. 2020. "Interictal Fast Ripples Are Associated With the Seizure-Generating Lesion in Patients With Dual Pathology." *Frontiers in Neurology* 11 (September): 573975. Accessed April 12, 2023. https://doi.org/10.3389/fneur.2020.573975.

Shih, Jerry J., Dean J. Krusienski, and Jonathan R. Wolpaw. 2012. "Brain-Computer Interfaces in Medicine" [in en]. *Mayo Clinic Proceedings* 87, no. 3 (March): 268–279. Accessed October 20, 2023. https://doi.org/10.1016/j.mayocp.2011.12.008.

Shokoueinejad, Mehdi, Dong-Wook Park, Yei Jung, Sarah Brodnick, Joseph Novello, Aaron Dingle, Kyle Swanson, et al. 2019. "Progress in the Field of Micro-Electrocorticography" [in en]. *Micromachines* 10, no. 1 (January): 62. Accessed April 18, 2023. https://doi.org/10.3390/mi10010062.

Siesjö, Bo K. 1972. "The regulation of cerebrospinal fluid pH." *Kidney international* 1 (5): 360–374.

Siesjö, Bo K., Roger von Hanwehr, Görel Nergelius, Gunilla Nevander, and Martin Ingvar. 1985. "Extra- and Intracellular pH in the Brain during Seizures and in the Recovery Period following the Arrest of Seizure Activity" [in en]. *Journal of*

Cerebral Blood Flow & Metabolism 5, no. 1 (March): 47–57. Accessed April 13, 2023. https://doi.org/10.1038/jcbfm.1985.7.

Sindhu, Kavyakantha Remakanthakurup, Duy Ngo, Hernando Ombao, Joffre E Olaya, Daniel W Shrey, and Beth A Lopour. 2023. "A novel method for dynamically altering the surface area of intracranial EEG electrodes." *Journal of Neural Engineering* 20, no. 2 (April): 026002. Accessed December 13, 2023. https://doi.org/10.1088/1741-2552/acb79f.

Stead, Matt, Mark Bower, Benjamin H. Brinkmann, Kendall Lee, W. Richard Marsh, Fredric B. Meyer, Brian Litt, Jamie Van Gompel, and Greg A. Worrell. 2010. "Microseizures and the spatiotemporal scales of human partial epilepsy" [in en]. *Brain* 133, no. 9 (September): 2789–2797. Accessed April 18, 2023. https://doi.org/10.1093/brain/awq190.

Suarez-Perez, Alex, Gemma Gabriel, Beatriz Rebollo, Xavi Illa, Anton Guimerà-Brunet, Javier Hernández-Ferrer, Maria Teresa Martínez, Rosa Villa, and Maria V. Sanchez-Vives. 2018. "Quantification of Signal-to-Noise Ratio in Cerebral Cortex Recordings Using Flexible MEAs With Co-localized Platinum Black, Carbon Nanotubes, and Gold Electrodes." *Frontiers in Neuroscience* 12 (November 29, 2018): 862. Accessed November 14, 2023. https://doi.org/10.3389/fnins.2018.00862.

Sun, James, Katrina Barth, Shaoyu Qiao, Chia-Han Chiang, Charles Wang, Shervin Rahimpour, Michael Trumpis, et al. 2022. "Intraoperative microseizure detection using a high-density micro-electrocorticography electrode array" [in en]. *Brain Communications* 4, no. 3 (May): fcac122. Accessed April 18, 2023. https://doi.org/10.1093/braincomms/fcac122.

Sweet, Jennifer A., Alia M. Hdeib, Andrew Sloan, and Jonathan P. Miller. 2013. "Depths and grids in brain tumors: Implantation strategies, techniques, and complications" [in en]. *Epilepsia* 54, no. s9 (December): 66–71. Accessed December 21, 2023. https://doi.org/10.1111/epi.12447.

Tadel, François, Sylvain Baillet, John C. Mosher, Dimitrios Pantazis, and Richard M. Leahy. 2011. "Brainstorm: A User-Friendly Application for MEG/EEG Analysis" [in en]. *Computational Intelligence and Neuroscience* 2011:1–13. Accessed July 12, 2023. https://doi.org/10.1155/2011/879716.

Tang, Yitian, Lijie Zhong, Wei Wang, Ying He, Tingting Han, Longbin Xu, Xiaocheng Mo, et al. 2022. "Recent Advances in Wearable Potentiometric pH Sensors" [in en]. *Membranes* 12, no. 5 (May): 504. Accessed December 19, 2023. https://doi.org/10.3390/membranes12050504.

Tchoe, Youngbin, Andrew M. Bourhis, Daniel R. Cleary, Brittany Stedelin, Jihwan Lee, Karen J. Tonsfeldt, Erik C. Brown, et al. 2022. "Human brain mapping with multithousand-channel PtNRGrids resolves spatiotemporal dynamics." *Science Translational Medicine* 14, no. 628 (January 19, 2022): eabj1441. Accessed October 12, 2023. https://doi.org/10.1126/scitranslmed.abj1441.

Thielen, Brianna, and Ellis Meng. 2021. "A comparison of insertion methods for surgical placement of penetrating neural interfaces." *Journal of Neural Engineering* 18, no. 4 (August): 041003. Accessed October 26, 2023. https://doi.org/10.1088/1741-2552/abf6f2.

Tian, Huihui, Ke Xu, Liang Zou, and Ying Fang. 2022. "Multimodal neural probes for combined optogenetics and electrophysiology" [in en]. *iScience* 25, no. 1 (January): 103612. Accessed December 21, 2023. https://doi.org/10.1016/j.isci.2021.103612.

Tiwari, Shivani, Varsha Sharma, Mubarak Mujawar, Yogendra Kumar Mishra, Ajeet Kaushik, and Anujit Ghosal. 2019. "Biosensors for Epilepsy Management: State-of-Art and Future Aspects." *Sensors* 19, no. 7 (March 28, 2019): 1525. Accessed March 27, 2023. https://doi.org/10.3390/s19071525.

Tolner, Else A, Daryl W Hochman, Pekka Hassinen, Jakub Otáhal, Eija Gaily, Michael M Haglund, Hana Kubová, Sebastian Schuchmann, Sampsa Vanhatalo, and Kai Kaila. 2011. "Five percent CO2 is a potent, fast-acting inhalation anticonvulsant." *Epilepsia* 52 (1): 104–114.

Tortora, Gerard J., and Bryan Derrickson. 2020. *Principles of anatomy and physiology.* Sixteenth edition. Hoboken, NJ: Wiley.

Traub, Roger D, Friederike Moeller, Richard Rosch, Torsten Baldeweg, Miles A Whittington, and Stephen P Hall. 2020. "Seizure initiation in infantile spasms vs. focal seizures: proposed common cellular mechanisms." *Reviews in the Neurosciences* 31 (2): 181–200.

Turski, Waldemar A., Esper A. Cavalheiro, Michael Schwarz, Stanisław J. Czuczwar, Zdzisław Kleinrok, and Lechosław Turski. 1983. "Limbic seizures produced by pilocarpine in rats: Behavioural, electroencephalographic and neuropathological study." *Behavioural Brain Research* 9, no. 3 (September): 315–335. https://doi.org/10.1016/0166-4328(83)90136-5.

Tybrandt, Klas, Dion Khodagholy, Bernd Dielacher, Flurin Stauffer, Aline F. Renz, György Buzsáki, and János Vörös. 2018. "High-Density Stretchable Electrode Grids for Chronic Neural Recording" [in en]. *Advanced Materials* 30, no. 15 (April): 1706520. Accessed October 24, 2023. https://doi.org/10.1002/adma.201706520.

Van Gompel, Jamie J., S. Matthew Stead, Caterina Giannini, Fredric B. Meyer, W. Richard Marsh, Todd Fountain, Elson So, Aaron Cohen-Gadol, Kendall H. Lee, and Gregory A. Worrell. 2008. "Phase I trial: safety and feasibility of intracranial electroencephalography using hybrid subdural electrodes containing macro- and microelectrode arrays." *Neurosurgical Focus* 25, no. 3 (September): E23. Accessed April 18, 2023. https://doi.org/10.3171/FOC/2008/25/9/E23.

Venkatraman, Subramaniam, Jeffrey Hendricks, Zachary A. King, Andrew J. Sereno, Sarah Richardson-Burns, David Martin, and Jose M. Carmena. 2011. "In Vitro and In Vivo Evaluation of PEDOT Microelectrodes for Neural Stimulation and Recording." *IEEE Transactions on Neural Systems and Rehabilitation Engineering* 19, no. 3 (June): 307–316. Accessed March 27, 2023. https://doi.org/10.1109/TNSRE.2011.2109399.

Viventi, Jonathan, Dae-Hyeong Kim, Leif Vigeland, Eric S Frechette, Justin A Blanco, Yun-Soung Kim, Andrew E Avrin, et al. 2011. "Flexible, foldable, actively multiplexed, high-density electrode array for mapping brain activity in vivo" [in en]. *Nature Neuroscience* 14, no. 12 (December): 1599–1605. Accessed October 24, 2023. https://doi.org/10.1038/nn.2973.

Vomero, Maria, Maria Francisca Porto Cruz, Elena Zucchini, Francesca Ciarpella, Emanuela Delfino, Stefano Carli, Christian Boehler, et al. 2020. "Conformable polyimide-based microECoGs: Bringing the electrodes closer to the signal source." *Biomaterials* 255 (October): 120178. Accessed March 27, 2023. https://doi.org/10.1016/j.biomaterials.2020.120178.

Voorhies, JasonM, and Aaron Cohen-Gadol. 2013. "Techniques for placement of grid and strip electrodes for intracranial epilepsy surgery monitoring: Pearls and pitfalls" [in en]. *Surgical Neurology International* 4 (1): 98. Accessed December 21, 2023. https://doi.org/10.4103/2152-7806.115707.

Wang, Yang, Xinze Yang, Xiwen Zhang, Yijun Wang, and Weihua Pei. 2023. "Implantable intracortical microelectrodes: reviewing the present with a focus on the future" [in en]. *Microsystems & Nanoengineering* 9, no. 1 (January): 7. Accessed December 21, 2023. https://doi.org/10.1038/s41378-022-00451-6.

Wise, K.D., A.M. Sodagar, Ying Yao, M.N. Gulari, G.E. Perlin, and K. Najafi. 2008. "Microelectrodes, Microelectronics, and Implantable Neural Microsystems." *Proceedings of the IEEE* 96, no. 7 (July): 1184–1202. Accessed December 21, 2023. https://doi.org/10.1109/JPROC.2008.922564.

Worrell, G.A., K. Jerbi, K. Kobayashi, J.M. Lina, R. Zelmann, and M. Le Van Quyen. 2012. "Recording and analysis techniques for high-frequency oscillations" [in en].

Progress in Neurobiology 98, no. 3 (September): 265–278. Accessed April 18, 2023. https://doi.org/10.1016/j.pneurobio.2012.02.006.

Worrell, Greg A., Andrew B. Gardner, S. Matt Stead, Sanqing Hu, Steve Goerss, Gregory J. Cascino, Fredric B. Meyer, Richard Marsh, and Brian Litt. 2008. "High-frequency oscillations in human temporal lobe: simultaneous microwire and clinical macroelectrode recordings" [in en]. *Brain* 131, no. 4 (April): 928–937. Accessed July 12, 2023. https://doi.org/10.1093/brain/awn006.

Yang, Xiao-Fan, Xiu-Yu Shi, Jun Ju, Wei-Na Zhang, Yu-Jie Liu, Xiao-Yan Li, and Li-Ping Zou. 2014. "5% CO2 inhalation suppresses hyperventilation-induced absence seizures in children." *Epilepsy research* 108 (2): 345–348.

Yeh, Hsiang-Lan, Jonathan V Garich, Ian R Akamine, Jennifer M Blain-Christen, and Seth A Hara. 2020. "Laser Micromachining of Thin-Film Polyimide Microelectrode Arrays: Alternative Processes to Photolithography." In *Frontiers in Biomedical Devices,* vol. 83549, V001T04A002. American Society of Mechanical Engineers.

Zhao, Fan, Yuandong Liu, Hui Dong, Shiqing Feng, Guoyue Shi, Longnian Lin, and Yang Tian. 2020. "An Electrochemophysiological Microarray for Real-Time Monitoring and Quantification of Multiple Ions in the Brain of a Freely Moving Rat." *Angewandte Chemie* 132 (26): 10512–10516.

Ziemann, Adam E, Mikael K Schnizler, Gregory W Albert, Meryl A Severson, Matthew A Howard Iii, Michael J Welsh, and John A Wemmie. 2008. "Seizure termination by acidosis depends on ASIC1a" [in en]. *Nature Neuroscience* 11, no. 7 (July): 816–822. Accessed August 7, 2023. https://doi.org/10.1038/nn.2132.

Zijlmans, Maeike, Premysl Jiruska, Rina Zelmann, Frans S.S. Leijten, John G.R. Jefferys, and Jean Gotman. 2012. "High-frequency oscillations as a new biomarker in epilepsy" [in en]. *Annals of Neurology* 71, no. 2 (February): 169–178. Accessed December 21, 2023. https://doi.org/10.1002/ana.22548.

APPENDIX A

IACUC APPROVAL

Institutional Animal Care and Use Committee (IACUC)
Office of Research Integrity and Assurance
Arizona State University
660 South Mill Avenue, Suite 312
Tempe, Arizona 85287-6111
Phone: (480) 965-6788 *FAX:* (480) 965-7772

Animal Protocol Review

ASU Protocol Number:	**18-1629R RFC 5**
Protocol Title:	**Multimodal Neural Interfaces**
Principal Investigator:	**Jennifer Blain Christen**
Date of Action:	**11/30/2020**

The animal protocol review was considered by the Committee and the following decisions were made:

The request for changes was approved by Designated Review to add additional procedures and Yuna Jung and Shiyi Liu as additional personnel to the protocol.

NOTE: If you have not already done so, documentation of Level III Training (i.e., procedure-specific training) will need to be provided to the IACUC office before participants can perform procedures without supervision. For more information on Level III requirements see https://researchintegrity.asu.edu/animals/training, or contact Research Support Services within DACT at dactrss@asu.edu.

Additional requirements:

☐ This protocol requires that DACT provide supervision for the first time a procedure is conducted. Contact dactrss@asu.edu to schedule.

☐ This protocol indicates that there are surgical procedures. A surgical checklist may be required to be submitted to Research Support Services within DACT (dactrss@asu.edu), prior to starting surgeries.

☐ Other requirements:

Total # of Animals:	**425**	
Species:	**Rats**	**Unalleviated Pain/Distress: No**
Protocol Approval Period:	**2/22/2018 – 2/21/2021**	
Sponsor:	**N/A**	
ASU Proposal/Award #:	**N/A**	
Title:	**N/A**	

Signature: Nicole Shepherd for N.Henderson Date: 12/1/2020
IACUC Chair or Designee

Cc: IACUC Office
IACUC Chair